Stability and dynamics of the laminar wake past a slender blunt-based axisymmetric body

P. BOHORQUEZ[1]**, E. SANMIGUEL-ROJAS**[1]**, A. SEVILLA**[2]**,
J. I. JIMÉNEZ-GONZÁLEZ**[1] **AND C. MARTÍNEZ-BAZÁN**[1]†

[1]Área de Mecánica de Fluidos, Departamento de Ingeniería Mecánica y Minera, Universidad Jaén,
Campus de las Lagunillas, 23071 Jaén, Spain

[2]Área de Mecánica de Fluidos, Departamento de Ingeniería Térmica y de Fluidos, Universidad
Carlos III de Madrid, 28911 Leganés, Spain

We investigate the stability properties and flow regimes of laminar wakes behind slender cylindrical bodies, of diameter D and length L, with a blunt trailing edge at zero angle of attack, combining experiments, direct numerical simulations and local/global linear stability analyses. It has been found that the flow field is steady and axisymmetric for Reynolds numbers below a critical value, $Re_{cs}(L/D)$, which depends on the length-to-diameter ratio of the body, L/D. However, in the range of Reynolds numbers $Re_{cs}(L/D) < Re < Re_{co}(L/D)$, although the flow is still steady, it is no longer axisymmetric but exhibits planar symmetry. Finally, for $Re > Re_{co}$, the flow becomes unsteady due to a second oscillatory bifurcation which preserves the reflectional symmetry. In addition, as the Reynolds number increases, we report a new flow regime, characterized by the presence of a secondary, low frequency oscillation while keeping the reflectional symmetry. The results reported indicate that a global linear stability analysis is adequate to predict the first bifurcation, thereby providing values of Re_{cs} nearly identical to those given by the corresponding numerical simulations. On the other hand, experiments and direct numerical simulations give similar values of Re_{co} for the second, oscillatory bifurcation, which are however overestimated by the linear stability analysis due to the use of an axisymmetric base flow. It is also shown that both bifurcations can be stabilized by injecting a certain amount of fluid through the base of the body, quantified here as the bleed-to-free-stream velocity ratio, $C_b = W_b/W_\infty$.

Key words: flow control, instability control, wakes

1. Introduction

Many aspects of the sequence of transitions leading to turbulence in wakes behind bluff bodies remain imperfectly understood. Their importance in engineering, together with their presence in many natural phenomena, justifies the intense work devoted to the dynamics of wakes in the laminar, transitional and turbulent regimes (Oertel 1990; Williamson 1996), as well as the effort to develop different strategies to control their behaviour (Choi, Jeon & Kim 2008). It is noteworthy that the considerable progress achieved towards these goals in the last few decades has been possible

† Email address for correspondence: cmbazan@ujaen.es

thanks to the combined use of experimental, numerical and hydrodynamic stability techniques. In particular, these efforts have provided a reasonably complete picture of many relevant features of wakes behind two-dimensional bluff bodies. However, except for the wakes behind spheres and disks, both of which have been the subject of a considerable number of experimental, numerical and stability studies, wakes behind other axisymmetric bluff bodies have been comparatively less studied despite their practical importance.

Wakes of axisymmetric objects undergo a rich sequence of transitions for increasing values of the Reynolds number prior to becoming turbulent. Thus, for instance, it is known that the wake of the sphere exhibits a first steady axisymmetry-breaking bifurcation at $Re \simeq 210$, followed by a second oscillatory one at $Re \simeq 277$ (Taneda 1956; Margavey & Bishop 1961; Levi 1980; Kim & Durbin 1988; Sakamoto & Haniu 1990; Ghidersa & Dušek 2000; Brückner 2001; Fabre, Auguste & Magnaudet 2008). Monkewitz (1988) showed that the first azimuthal mode $|m| = 1$ can become locally absolutely unstable in the near wake of axisymmetric bluff bodies, and found that the typical frequencies and wavenumbers associated with this absolute instability were close to those observed experimentally at high Reynolds numbers as large-scale helical structures (Achenbach 1974; Taneda 1978; Fuchs, Mercker & Michel 1979; Berger, Scholz & Schumm 1990). Afterwards, Natarajan & Acrivos (1993) showed through a global linear stability analysis that the two successive bifurcations were both a consequence of the destabilization of the first azimuthal instability mode of the basic axisymmetric steady flow. Moreover, Natarajan & Acrivos (1993) indicated that the wake behind a disk supported the same linear instability modes, only differing in the corresponding values of the critical Reynolds numbers. These findings were confirmed and extended by the weakly nonlinear analyses recently performed by Fabre *et al.* (2008) and Meliga, Chomaz & Sipp (2009). On the experimental side, Ormiéres & Provansal (1999) demonstrated that the second transition to periodic vortex shedding was a supercritical Hopf bifurcation described by the Stuart–Landau equation. The experiments of Brückner (2001) showed later that wakes behind bullet-shaped bodies with a blunt trailing edge undergo the same basic bifurcations as the sphere and the disk, but take place at higher Reynolds numbers.

Base-bleed control of the turbulent wake of an axisymmetric blunt-based object was studied experimentally and with a local linear stability analysis by Sevilla & Martínez-Bazán (2004, 2006). In particular, Sevilla & Martínez-Bazán (2004) found that local absolute instability can be suppressed for bleed coefficients larger than a certain critical value, in agreement with the inhibition of large-scale helical vortex shedding observed in the corresponding experiments. The applicability of local stability theory to predict the critical bleed coefficient can be justified by noting that, while the base flow is strongly non-parallel in the case without base bleed, it becomes slender for bleed coefficients near the critical one. A similar configuration has recently been studied by Sanmiguel-Rojas *et al.* (2009) in the laminar regime by means of a global stability analysis, finding the existence of critical values of the bleed coefficient to restabilise both the steady and oscillatory global modes for moderately high supercritical Reynolds numbers (see also Meliga, Sipp & Chomaz 2010*b*).

It must be emphasized that the application of local stability concepts is questionable in the case of strongly non-parallel flows. Indeed, for instance, the results of Pier (2008) for the wake of a sphere clearly showed that the theory of nonlinear global modes developed for weakly non-parallel flows (Pier *et al.* 1998) fails in predicting the onset of global oscillations. In such cases, either direct numerical simulations or global stability

analyses must be made in order to obtain quantitatively reliable results. In particular, a detailed nonlinear description of the sequence of bifurcations which take place for increasing Reynolds numbers in the flow around axisymmetric bodies has been possible only recently. Thus, Schwarz & Bestek (1994) performed direct numerical simulations of the laminar flow around a bullet-shaped body at Reynolds numbers 500 and 1000, showing that the dynamics of the wake is controlled by a global instability of large-scale helical instability modes, resulting from the simultaneous destabilization and subsequent nonlinear interaction of a pair of counter-rotating $m = \pm 1$ azimuthal modes. Afterwards, Johnson & Patel (1999) and Tomboulides & Orszag (2000) carried out direct numerical simulations of the flow past a sphere showing very good agreement with the global stability analysis of Natarajan & Acrivos (1993) within the linear regime. Ghidersa & Dušek (2000) provided a nonlinear theory for both the axisymmetry-breaking and oscillatory bifurcations in the wake of the sphere, and performed direct numerical simulations of the linearized and fully nonlinear Navier–Stokes equations, showing good agreement with the previous works (see also Pier 2008). The direct numerical simulations due to Kim & Choi (2003) for the flow past a hemisphere revealed that, after the first steady symmetry-breaking bifurcation, the subsequent Hopf bifurcation does not preserve the symmetry plane. A third bifurcation takes place at a higher critical Reynolds number, in which a plane of symmetry reappears, and, finally, a fourth bifurcation leads to an aperiodic state. This phenomenology was later found to apply also to the wake of a thin disk by Fabre *et al.* (2008) and Shenoy & Kleinstreuer (2008). In addition, numerical simulations of the flow around a thick disk with length-to-diameter ratio 1/3 have been performed by Auguste *et al.* (2010), providing a detailed description of the subsequent nonlinear states leading to the appearance of chaos in the wake. Auguste *et al.* (2010) identified a sequence of states considerably more complex than the corresponding scenario for the infinitely thin disk, including regimes previously unobserved in other geometries.

A theoretical explanation of the different nonlinear states observed in experiments and numerical simulations has been given recently for the wakes of a sphere and an infinitely thin disk by Fabre *et al.* (2008), and by Auguste *et al.* (2010) for the thick disk case. In particular, Fabre *et al.* (2008) and Auguste *et al.* (2010) took advantage of the fact that the Reynolds numbers associated with the first two bifurcations are close to each other to develop a weakly nonlinear description based on multiple codimension bifurcation theory (Golubitsky, Stewart & Schaeffer 1988; Kuznetsov 1995), showing close agreement with direct numerical simulations. In addition, a first-principles calculation of the coefficients associated with the weakly nonlinear modal expansion has recently been given by Meliga *et al.* (2009) for the thin disk case, by means of the adjoint operator technique. Unfortunately, the theory of multiple codimension bifurcations applied to the wake of axisymmetric bodies (see Fabre *et al.* 2008; Meliga *et al.* 2009, and references therein) requires that the corresponding branches bifurcating from the original steady axisymmetric state are close enough, so that the amplitude of the nonlinear saturated state appearing after the first bifurcation is small. A possible measure of this distance is provided by the relative difference between the critical values of the Reynolds numbers associated with both instability modes, $\Delta = (Re_{co} - Re_{cs})/Re_{cs}$, where Re_{cs} and Re_{co} denote the critical Reynolds numbers corresponding to the steady and oscillatory bifurcations, respectively. In the case of the thin disk wake, the parameter $\Delta \ll 1$, and thus the normal form theory can be applied. However, it has recently been found by Sanmiguel-Rojas *et al.* (2009) that, for the wake of a blunt-based cylindrical body,

the parameter $\Delta \sim O(1)$, and the theory of multiple codimension bifurcations is thus questionable for this kind of body. Moreover, taking into account the substantial differences found between the thin and thick disk cases discussed above, it is expected that the wake of the slender blunt-based body will also present specific features, which are worth considering in detail given the practical importance of this geometry.

Therefore, the main objective of the present work is to perform a detailed study of the flow regimes taking place in the laminar wake of a blunt-based cylindrical body and their control by base-bleed, up to a Reynolds number of about 2000. The study combines experiments, direct numerical simulations and local/global linear stability analyses, thus extending our previous work on the problem (Sevilla & Martínez-Bazán 2004, 2006; Sanmiguel-Rojas *et al.* 2009). This paper is structured as follows. Section 2 is devoted to the presentation of the direct numerical simulation and experimental techniques used in this work. The results obtained for the particular case without base bleed, as well as the influence of the solid body aspect ratio on the stability properties of the flow, are presented and discussed in §3.1, and the stabilizing effect of base bleed will be addressed in §3.2. In addition, §§3.1 and 3.2 include results obtained using local and global linear stability techniques, indicating their limitations in this type of flow. Finally, §4 is devoted to conclusions and suggestions for future work.

2. Numerical and experimental techniques

2.1. *Three-dimensional numerical simulations*

The numerical simulations were performed with OpenFOAM® (http://www.openfoam.com), an open source computational fluid dynamics software package produced by OpenCFD Ltd. The flow configuration under study in this work consists of a uniform fluid stream of density ρ and viscosity μ flowing with a velocity W_∞ around a cylindrical body of diameter, D, and total length L with an ellipsoidal rounded nose, of 2:1 major-to-minor axis ratio, aligned with the direction of the free stream. To perform the three-dimensional, unsteady numerical simulations of the flow, we solved the dimensionless form of the standard incompressible Navier–Stokes equations,

$$\nabla \cdot \boldsymbol{u} = 0, \tag{2.1}$$

$$\frac{\partial \boldsymbol{u}}{\partial t} + \nabla \cdot (\boldsymbol{u}\boldsymbol{u}) + \nabla p - \frac{1}{Re}\nabla^2 \boldsymbol{u} = 0, \tag{2.2}$$

where $Re = \rho\,W_\infty\,D/\mu$ is the Reynolds number. The equations were made dimensionless, using D, W_∞, D/W_∞ and $\rho\,W_\infty^2$ as length, velocity, time and pressure scales respectively, in Cartesian coordinates although, for convenience, the results will be presented in cylindrical coordinates, (r, θ, z), with a velocity field given by $\boldsymbol{u} = (u, v, w)$ in the radial, azimuthal and axial directions respectively, and the origin of coordinates placed at the central point of the body base.

The full Navier–Stokes equations (2.1) and (2.2) were solved within the computational domain shown in figure 1, enclosed by five boundary surfaces. The flow inlet, denoted by Ω_i, which consists of a semi-sphere of diameter 20 times the diameter of the slender body, D, is followed by a tubular surface, Ω_f, that extends 50 diameters from the base of the body. The external boundary is closed by the outer plane, Ω_o, defined as the base of the tubular surface. Subsequently,
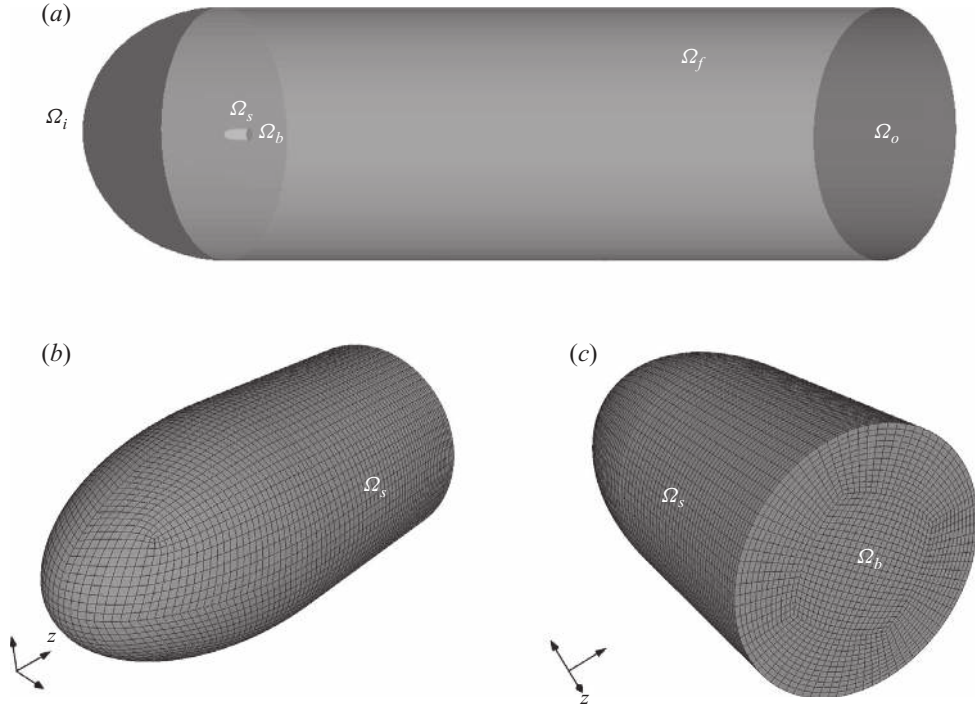
FIGURE 1. (*a*) Sketch and boundaries of the computational domain employed in the three-dimensional numerical simulations. Detail of the ellipsoidal bluff-body mesh and sketch of its boundaries (i.e. base and ellipsoidal surface, denoted by Ω_b and Ω_s, respectively): (*b*) frontal and (*c*) rear view.

the body was introduced at the centreline of the cylindrical domain, aligned with the direction of the free stream, as shown in figure 1(*a*). For notational clarity, the surface of the slender body was decomposed into two surfaces: the base, Ω_b, plus the remaining part of the solid surface, Ω_s. A detailed view of the solid boundaries and the corresponding surface mesh is also shown in figures 1(*b*) and 1(*c*). Furthermore, in order to validate both the computational domain, which consists of a three-dimensional mesh of nearly 3×10^6 hexahedras [$106(r) \times 60(\theta) \times 460(z)$], and the numerical schemes described below, we performed numerical simulations of the incompressible laminar flow around a sphere of diameter D. The results obtained for the critical Reynolds numbers of the first-steady bifurcation, $Re_{cs} \simeq 209.6$, and the second-oscillatory one, $276 < Re_{co} < 277$, are in excellent agreement with previous results reported by other researchers (Johnson & Patel 1999; Ghidersa & Dušek 2000; Tomboulides & Orszag 2000; Magnaudet & Mougin 2007).

The present computational domain is similar to those employed in the previous numerical studies of the flow around a sphere (Johnson & Patel 1999; Ghidersa & Dušek 2000; Tomboulides & Orszag 2000; Magnaudet & Mougin 2007) and hemisphere (Kim & Choi 2003), where the non-dimensional spatial domain along the upstream and the radial directions from the body varied from 9 to 25 and from 8 to 25, respectively, whilst the length downstream from the sphere usually takes values between 25 and 30. Furthermore, Sanmiguel-Rojas *et al.* (2009) showed in their global stability analyses that the eigenvalue spectrum obtained for a

cylindrical body similar to that considered here was nearly independent of the length and the width of the computational domain for the domains employed in our computations.

Equations (2.1) and (2.2) were solved with the following boundary conditions (see figure 1):

$$u(x, t) = 0, \quad x \in \Omega_s, \quad t > 0, \tag{2.3}$$

$$u(x, t) = (0, 0, 1)^{\mathrm{T}}, \quad x \in \Omega_i, \quad t > 0, \tag{2.4}$$

$$u(x, t) = (0, 0, C_b)^{\mathrm{T}}, \quad x \in \Omega_b, \quad t > 0, \tag{2.5}$$

$$n \cdot u(x, t) = 0, \quad x \in \Omega_f, \quad t > 0, \tag{2.6}$$

$$p(x, t) = n \cdot \nabla u(x, t) = 0, \quad x \in \Omega_o, \quad t > 0, \tag{2.7}$$

where we assumed a free stream of uniform velocity profile at the inlet of the computational domain, Ω_i (2.4), and allowed a uniform injection of fluid throughout the base of the slender body, Ω_b, of velocity $C_b = W_b/W_\infty$, which denotes the bleed-to-free-stream velocity ratio, referred to as *bleed coefficient* (2.5). On the other hand, we imposed slip boundary condition at Ω_f, given by (2.6), where n is the normal surface vector pointing outwards from the computational domain. The pressure values in the boundary conditions (2.3)–(2.6) are implicitly obtained through the continuity equation (2.1) (as described by Ferziger & Perić 2002), and it is set constant at the outlet, Ω_o (2.7), see Tomboulides & Orszag (2000). Nevertheless, this boundary condition at Ω_o was also supplemented with a Neumann boundary condition for the velocity vector. Details of the numerical schemes implemented can be found in Appendix A.

2.2. *Experimental details*

The velocity measurements of the wake behind an axisymmetric slender body with an elliptical nose of 2:1 major-to-minor axis ratio and a sharp trailing edge were performed in a vertical wind tunnel of 20×20 cm^2 cross-section. Different bodies of diameter $D = 1$ cm, and length-to-diameter ratios $L/D = 1, 2, 3, 4$ and 6, respectively, were used to determine the effect of the boundary layer thickness at the separation point on the stability properties of the flow (see figures 2a and 2c). The body, which was aligned with the free stream, was held with a 1 mm external diameter hollow needle welded internally to the body at $z = -L/2D$ (the middle point of the body). After connecting the supporting needle, the junction was polished to obtain a smooth surface over the body. To verify that the holding device did not introduce any perturbation in the flow, we measured the velocity fluctuations at $r = 0.5$ and several downstream positions, and no oscillations were observed for $Re < Re_{co}$. Furthermore, considering the range of Reynolds numbers explored in this work, the Reynolds number based on the diameter of the supporting needle was smaller than 50 in most of the cases and, consequently, vortex shedding did not take place. Nevertheless, if vortex shedding took place, the shedding frequencies would be of the order of 200 Hz and no energy was observed in this range of frequencies in the energy spectra obtained experimentally. A hot-wire anemometer was used to measure the streamwise velocity, $w(t)$, at several downstream positions. The temperature was monitored to precisely calculate the density and viscosity of the air stream.

Base bleed was used as wake control mechanism to inhibit the emission of vortices from the base of the body. Thus, the supporting needle, also used to inject the control fluid, was connected to the air-feeding line and a hollow slender body as shown in figure 2(b). A piece of foam was inserted inside the body to generate a pressure
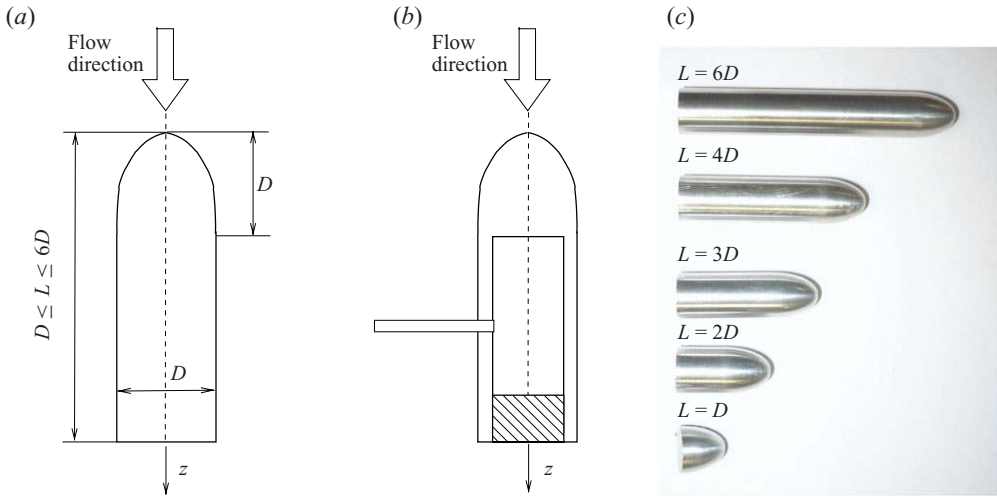
FIGURE 2. (Colour online) Shape of the axisymmetric body with a rounded ellipsoidal nose used in this work. (*a*) Solid body, (*b*) hollow body used in the experiments with base bleed and (*c*) image of the different solid bodies with length-to-diameter ratios $L/D = 1, 2, 3, 4$ and 6, respectively. The shaded area in (*b*) represents the piece of foam inserted to guarantee a uniform bleed velocity.

drop large enough to guarantee a uniform bleed velocity profile. The holding needle was connected through a Luer connector to the air-feeding line, which consisted of the pneumatic tube provided by an Aalborg$^{©}$ digital mass flowmeter, a precision valve used to precisely control the air flow rate injected and a pressure regulator. The feeding line was connected to the 6 bar compressed air line of our laboratory. To check the uniformity of the air flow injected through the base of the body, we measured the bleed velocity placing the hot-wire probe near the base of the body at different radial positions, getting almost identical values of anemometer output voltage. Additionally, we also performed shadowgraphs to visualize the bleed flow using helium to make sure that the flow was uniformly injected through the base of the body.

3. Results and discussion

We shall first describe in § 3.1 the sequence of transitions occurring in the wake of a body with length-to-diameter ratio $L/D = 2$ for increasing values of the Reynolds number, in the absence of base bleed. In addition, an analysis of the influence of L/D will be presented to close § 3.1. The details of the procedures used to determine the critical Reynolds numbers corresponding to the stationary and the oscillatory bifurcations are given in Appendix B. Subsequently, in § 3.2 we focus on a fixed body with $L/D = 2$, presenting a detailed analysis of the stabilising effect of base bleed. We show, in particular, that the axisymmetric base state can be recovered for $Re \leqslant 2000$ by injecting a sufficient amount of fluid through the body base. In both sections, we will discuss the results obtained from the numerical simulations, the global linear stability analysis and the experiments. Moreover, in § 3.2 we complete our work by discussing the validity of the local stability analysis to predict the critical bleed coefficient needed to inhibit the second oscillatory bifurcation.
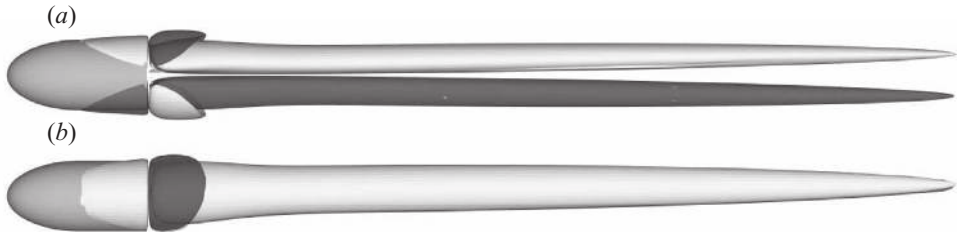
FIGURE 3. Contours of constant streamwise vorticity, $\omega_z = \pm 0.05$, for $Re = 350$: (*a*) plan and (*b*) side views. The figure shows that the flow is steady and exhibits planar symmetry.

3.1. *Description of the flow field and results without base bleed, $C_b = 0$*

According to our three-dimensional numerical simulations, the flow past a cylindrical body with an elliptical nose and length-to-diameter ratio 2 is axisymmetric for Reynolds numbers up to $Re_{cs}^{3d} \simeq 319$, where the flow experiences a first transition to a steady, non-axisymmetric state. Although for $Re > Re_{cs}^{3d}$ the wake no longer exhibits axial symmetry, it still remains steady for Reynolds numbers lower than $Re_{co}^{3d} \simeq 413$. Figure 3, which shows the isosurfaces corresponding to the positive (light) and negative (dark) values of the axial vorticity of $\omega_z = \pm 0.05$, illustrates the loss of axial symmetry at $Re = 350$. This regime is similar to that observed for the sphere and the disk for Reynolds numbers above 210 and 115, respectively, as a consequence of the destabilization of a global mode referred to as the *steady-state* (SS) mode according to Fabre *et al.* (2008). Note that the pair of steady streamwise vortices extends upstream of the solid-body base, indicating the global nature of the steady-state mode. The flow is characterized by a loss of axisymmetry, although it attains a state where planar symmetry is observed, as shown in figure 3(*a*). However, the view obtained by a 90° azimuthal rotation of the mesh, see figure 3(*b*), illustrates the fact that the streamwise vortices are not aligned with the streamwise direction but exhibit an increasingly larger eccentricity as we move further downstream from the solid base, similar to the sphere and disk wakes (e.g. Ormiéres & Provansal 1999; Tomboulides & Orszag 2000; Thompson, Leweke & Provansal 2001; Schouveiler & Provansal 2002). The dependence of the eccentricity on the Reynolds number has been quantified in Appendix B to provide a precise description of the method used to determine the onset of the SS mode for our bullet-shaped geometry (see also Mullin *et al.* 2009). In addition to performing the three-dimensional numerical simulations, we also carried out global stability analyses of the same geometrical configuration, obtaining a critical Reynolds number of $Re_{cs}^{GLS} \simeq 327$ for the first bifurcation, which differs from that given by the numerical simulations, $Re_{cs}^{3d} \simeq 319$, only by about 2.5 %. The results obtained by the global linear stability analysis for $Re = 350$ and $|m| = 1$ have been represented in figure 4. Specifically, figure 4(*a*) indicates that, in agreement with the numerical simulations, at $Re = 350$ the spectrum exhibits only one unstable eigenvalue ($\sigma_r > 0$) which corresponds to a three-dimensional ($|m| = 1$) and steady ($\sigma_i = 0$) perturbation. The associated normalized eigenfunctions are plotted in figure 4(*b*), showing the presence of two counter-rotating streamwise vortices aligned within the streamwise direction. Details of the numerical schemes used to perform the global stability analyses can be found in Appendix A.

By increasing the Reynolds number in the three-dimensional numerical simulations above $Re_{co}^{3d} = 413$, we observe the development of a second transition to an oscillatory mode which retains the planar (or reflectional) symmetry due to the destabilization
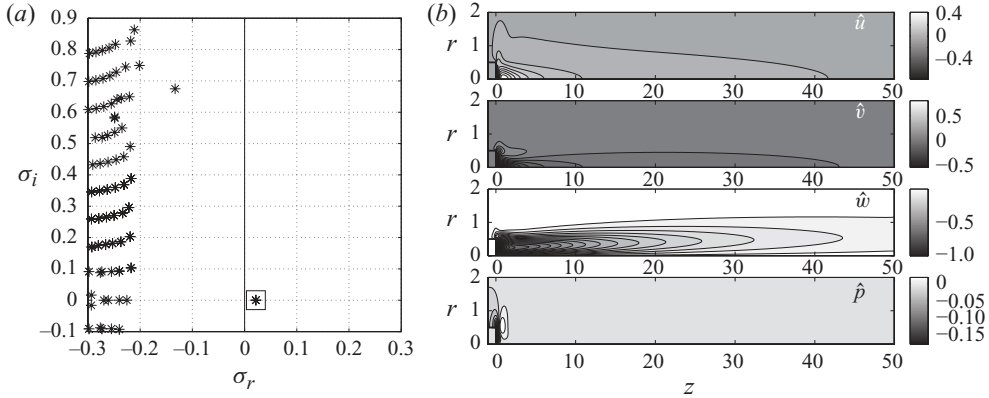
FIGURE 4. (a) Eigenvalue spectrum for $Re = 350$, $|m| = 1$ and $L/D = 2$. (b) Isolines of the real part of the normalized eigenfunctions $\hat{u}$, $\hat{v}$, $\hat{w}$ and $\hat{p}$ for the eigenvalue marked with a square in (a). The eigenfunctions have been normalized with $\|\hat{\boldsymbol{q}}\|_{\infty}$.
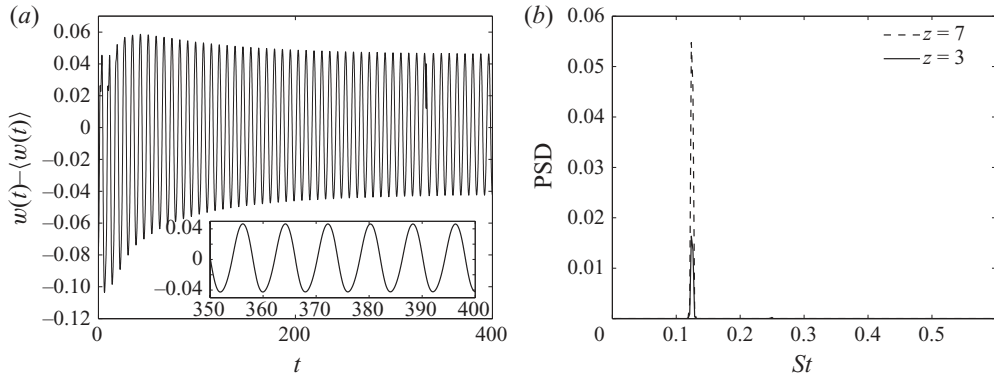

FIGURE 5. (a) Time history of the fluctuations of the streamwise velocity component, $w(t) - \langle w(t) \rangle$, obtained numerically at $(0,0,7)$ for $Re = 415$. The inset in (a) shows a monochromatic signal, as corroborated by the power spectral density shown in (b) at $z = 7$ and $z = 3$ for $t > 500$.

of a *reflectional symmetry preserving* (RSP) mode according to Fabre *et al.* (2008). It is worth pointing out that in the present work we shall make use of the notation employed by Fabre *et al.* (2008), although Meliga *et al.* (2009) and Auguste *et al.* (2010) referred to the RSP mode as MM0 and zig-zig, respectively. Figure 5 shows the streamwise velocity signal recorded at the symmetry axis for $Re = 415$ and $z = 7$, as well as the corresponding power spectral density (PSD) function for $t > 500$, which is obtained after removing the time-averaged streamwise velocity, defined here as $\langle w(t) \rangle = T^{-1} \int_{t}^{t+T} w(t)\, dt$. As in the case of the sphere (Schouveiler & Provansal 2002), monochromatic vortices are shed for Reynolds numbers slightly larger than Re_{co}^{3d}. Subsequently, the vortex-shedding Strouhal number (St) is about 0.1246 and lies very close to the experimental value of 0.1231 obtained for the same geometry near the critical Reynolds number (see also figure 10). Similar to the case of the steady planar-symmetric regime, the vorticity contours provide a clear picture for the structure of the wake. Figures 6 and 7 show an analogous view to figures 3(a) and 3(b), respectively, at four phases ϕ of the vortex shedding
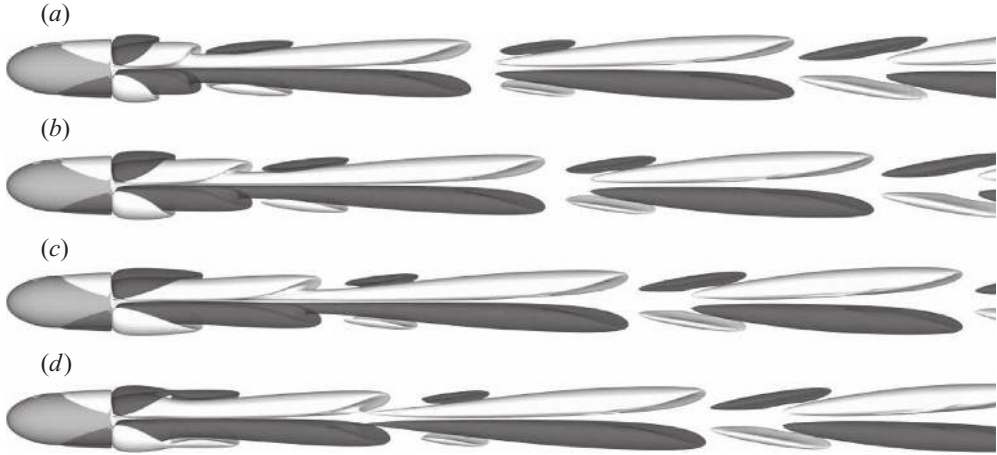
(*a*)

(*b*)

(*c*)

(*d*)

FIGURE 6. Plan view of streamwise vorticity contours, $\omega_z = \pm 0.05$, close to criticality for $Re = 415$ at every quarter period: (*a*) $\phi = 0$, (*b*) $\phi = \pi/4$, (*c*) $\phi = \pi$ and (*d*) $\phi = 3\pi/4$. See supplementary movie 1.
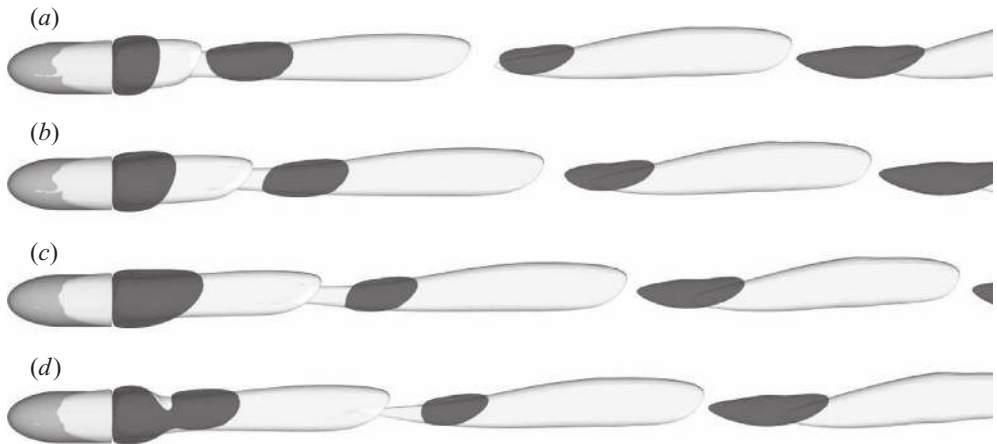
(*a*)

(*b*)

(*c*)

(*d*)

FIGURE 7. Side view of the streamwise vorticity contour, $\omega_z = \pm 0.05$, as for figure 6: (*a*) $\phi = 0$, (*b*) $\phi = \pi/4$, (*c*) $\phi = \pi$ and (*d*) $\phi = 3\pi/4$.

cycle (see supplementary movie 1 available at journals.cambridge.org/flm). However, the global stability analysis predicts the oscillatory bifurcation for $Re_{co}^{GLS} \simeq 518$, thus showing a significant difference with respect to both the numerical simulations and the experiments, where $Re_{co}^{3d} \simeq 413$ and $Re_{co}^{exp} \simeq 412.4$, respectively (see below). It is important to emphasise that this overprediction in the critical Reynolds number of the second bifurcation is due to the use of an axisymmetric basic flow for Reynolds numbers higher than that corresponding to the first, steady bifurcation. Note that, at supercritical Reynolds numbers, $Re > Re_{cs}$, the original basic flow is already perturbed and, in particular, is no longer axisymmetric due to the three-dimensional nature of the first bifurcation mode, $|m| = 1$. Figure 8(*a*) shows the spectrum for $Re_{co}^{GLS} \simeq 518$, where the eigenvalue corresponding to the unstable oscillatory mode has been marked with a circle. This second transition corresponds to a three-dimensional, $|m| = 1$, and oscillating perturbation with a Strouhal number $St = \sigma_i/2\pi \approx 0.102$,
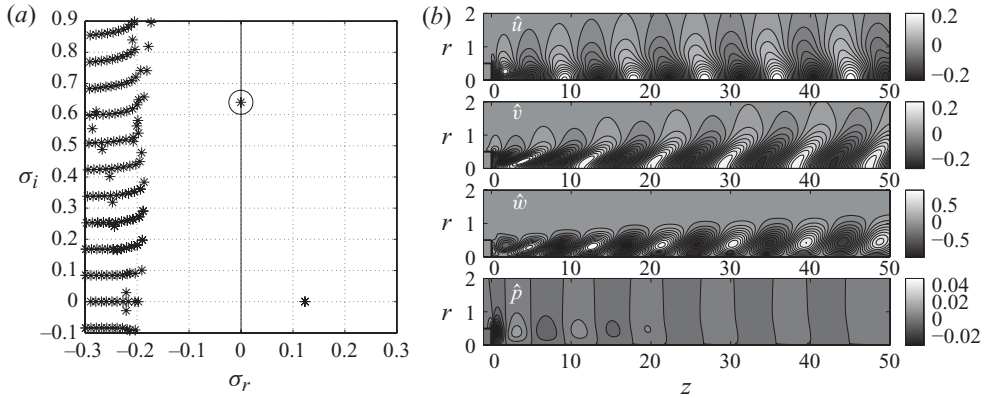
FIGURE 8. (a) Eigenvalue spectrum for $Re = 518$, $|m| = 1$ and $L/D = 2$. (b) Isolines of the real part of the normalized eigenfunctions $\hat{u}$, $\hat{v}$, $\hat{w}$ and $\hat{p}$ for the eigenvalue marked with a circle in (a). The eigenfunctions have been normalized with $\|\hat{\boldsymbol{q}}\|_\infty$.
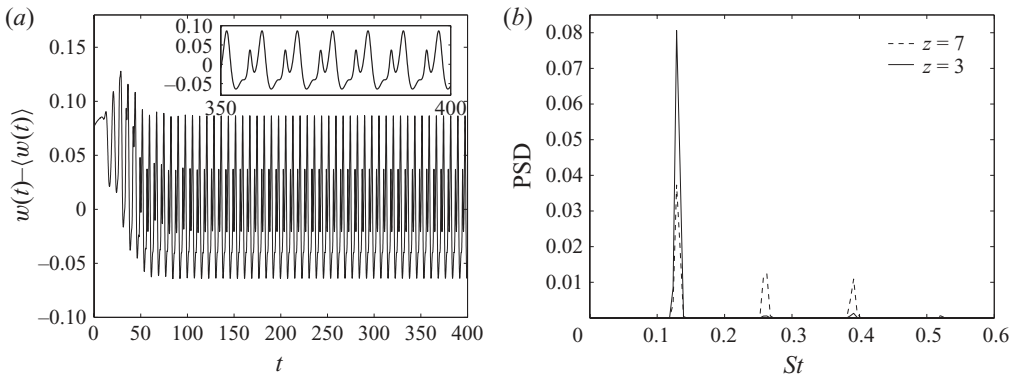

FIGURE 9. (a) Time history of the fluctuations of the streamwise velocity component, $w(t) - \langle w(t) \rangle$, obtained numerically at $(0,0,7)$ for $Re = 450$. The presence of harmonics is illustrated in the inset of (a) as well as in (b), which shows the PSD at $z = 3$ and $z = 7$.

whose associated normalized eigenfunctions have been plotted in figure 8(b), showing a spatially periodic structure similar to that obtained in the numerical simulations. The discrepancy between the vortex-shedding Strouhal numbers obtained from the global stability analysis and the numerical simulations indicates that the exact structure of the global modes and their temporal frequency must be determined by means of a three-dimensional global stability analysis as described by Bagheri *et al.* (2009), though such task is outside the scope of the present paper.

The single-frequency vortex shedding process observed in our numerical simulations occurs up to $Re \simeq 450$ and the structure of the flow is similar to that reported for the sphere in the range of Reynolds number $285 < Re < 300$ by Tomboulides & Orszag (2000). For increasing values of $Re > 450$, we find the development of harmonics as shown in figure 9. Note that in the case of the flow past a sphere at $Re = 300$, the appearance of harmonics is clearer in the numerical simulations (Tomboulides & Orszag 2000) than in experiments (Schouveiler & Provansal 2002). Therefore, the present numerical results qualitatively agree with previous known numerical results for the wake of a sphere. However, it is worth noting that the energy associated with
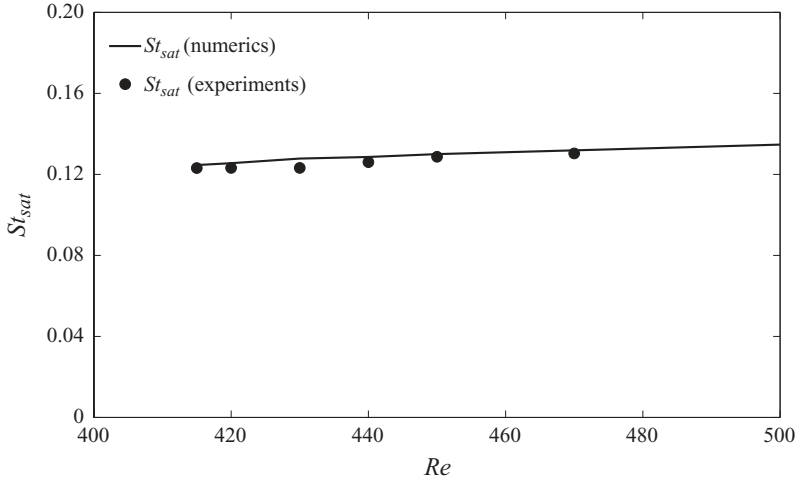
FIGURE 10. Comparison between the evolutions of the vortex-shedding Strouhal number, St_{sat}, with the Reynolds number, Re, obtained from the numerical simulations and experimental measurements for a body of aspect ratio $L/D = 2$.

the harmonics diminishes as we decrease the distance to the bluff-body base. For instance, figure 9(b) shows that their effect is negligible at $z = 3$, whilst their energy grows as we move downstream, for example at $z = 7$. Thus, in order to determine the Strouhal number corresponding to the primary frequency of the vortex shedding, St_{sat}, we have performed the spectral analysis of the streamwise velocity $w(t)$ at $(0, 0, 3)$, a position where the dominant frequency is more energetic, up to a Reynolds numbers of 500. The results shown in figure 10 indicate that the Strouhal number slightly increases with Re, a result which is consistent with the case of a sphere (e.g. Ormiéres & Provansal 1999; Schouveiler & Provansal 2002). This figure also shows the Strouhal numbers obtained experimentally, indicating the good agreement between the numerical and the experimental results.

Finally, we have also observed the development of marked oscillations upstream of the body base in the presence of vortex shedding, an effect that increases as the Reynolds number increases. In fact, the oscillations of velocity and pressure upstream of the solid-body base are clearly observed at moderate Reynolds numbers, e.g. $Re = 500$, and can be noted by plotting the vorticity contours. Thus, figure 11 illustrates the low-frequency shedding of vortices during four cycles; in the two first cycles, i.e. from $\phi = 0$ to 4π, it can be observed that the distribution of streamwise vorticity fluctuates smoothly on the solid surface, similar to what happens at Reynolds numbers close to criticality. Note that, at $\phi = \pi$, 3π, it is evident that the vorticity contours over the solid body oscillate in the streamwise direction and recover their initial state at $\phi = 2\pi$, 4π (these oscillations can be clearly seen in supplementary movie 2). Indeed, the vortices that are shed at this stage are similar to those described in figures 6 and 7 for $Re = 415$. The oscillations are more intense in the two consecutive periods and the ensuing vorticity contours differ from the previous ones which are convected downstream. This sequence is periodic, the phenomenon appearing in the numerical simulation every four cycles. The emission of low-frequency vortices is apparent in supplementary movie 2. Indeed, the PSD functions shown in figures 12(a) and 12(b) for the streamwise and tangential components of the velocity fluctuations respectively indicate that the predominant Strouhal numbers are those corresponding
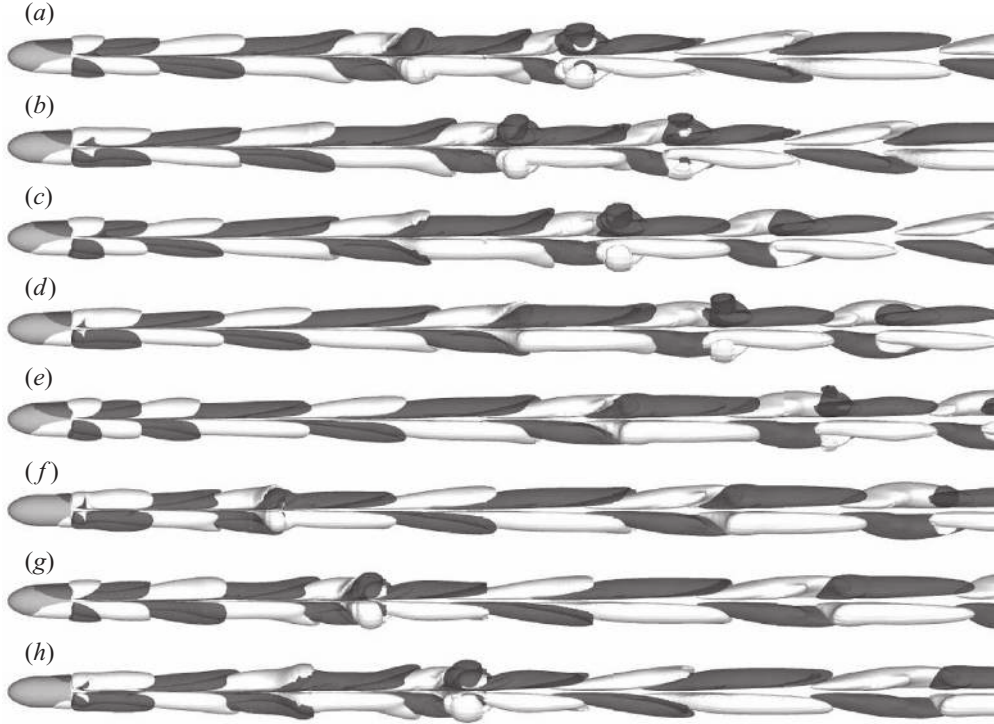
FIGURE 11. Plan view of streamwise vorticity contours, $\omega_z = \pm 0.05$, at $Re = 500$ at every half period: (*a*) $\phi = 0$, (*b*) $\phi = \pi$, (*c*) $\phi = 2\pi$, (*d*) $\phi = 3\pi$, (*e*) $\phi = 4\pi$, (*f*) $\phi = 5\pi$, (*g*) $\phi = 6\pi$ and (*h*) $\phi = 7\pi$. See supplementary movie 2.
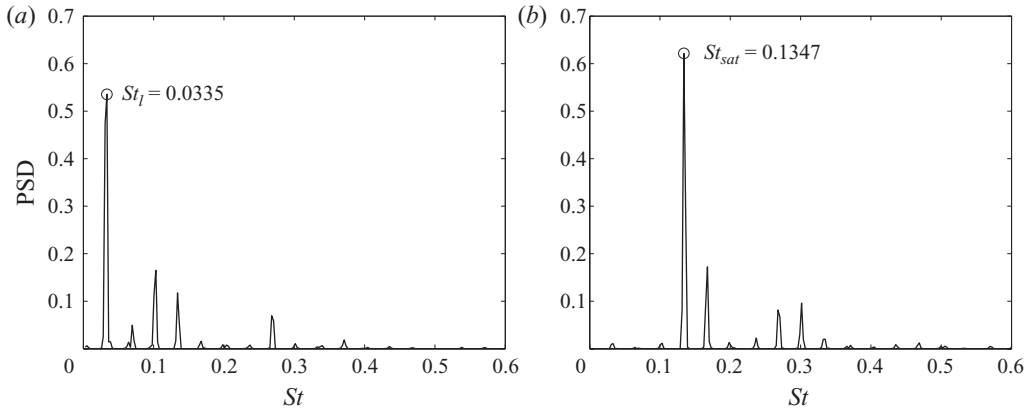

FIGURE 12. Power spectral density at $z = 7$ for $Re = 500$ corresponding to the (*a*) streamwise and (*b*) tangential velocity components given by the numerical simulations. The ratio between St_{sat} and St_l is approximately 4.02.

to the natural shedding frequency (denoted hereafter by St_{sat}) and, approximately, a quarter of St_{sat}, $St_l \approx St_{sat}/4$. Note that, here St_l resembles the low (or secondary) frequency observed for the flow past a sphere at $Re > 360$ which has been associated with the loss of the planar symmetry due to irregular variations in the azimuthal orientation of the vortex shedding, see Tomboulides & Orszag (2000, p. 65 and

figure 20*b*) and Schouveiler & Provansal (2002, p. 3851 and figure 9). However, unlike in the case of the sphere, the reflectional symmetry is maintained in the current scenario, as shown in figure 11. This flow regime is not yet fully described in the literature, but a brief mention of its existence in the wake of a sphere can be found in Bouchet, Mebarek & Dušek (2006) at $Re \sim 325$. A similar phenomenon has also been reported by Stewart *et al.* (2010) for a sphere rolling down an inclined wall, which exhibits dual spectral peaks at $Re = 225$ whilst the flow retains the symmetry plane. However, in such a case, the low frequency corresponds to $St_l = 0.045$, whilst the dominant frequency is $St_{sat} = 0.12$ for a lower Reynolds number of $Re = 212.5$, i.e. the secondary frequency is approximately one-third of the leading frequency. In addition, the wake of a thick circular disk is also characterised by the persistence of *planar symmetry* and the appearance of a secondary frequency close to one-third of the leading frequency for Reynolds numbers above 217 (Auguste *et al.* 2010). However, unlike in the present case, in the case of a thick disk this flow regime results after a sequence of bifurcations occurring at lower Reynolds numbers. Thus, techniques more complex than those used in the present work, like the global dynamic modes described in Schmid (2010), would be needed in order to better understand this complex flow behaviour. It is worth mentioning that the excitation of new frequencies in the wake (i.e. the low-frequency modulation and the harmonics of the main frequency) leads to a decrease of the energy associated with the leading velocity fluctuations due to the nonlinear energy transfer from the natural frequency St_{sat} to the newly excited ones.

In addition to performing three-dimensional numerical simulations, we also measured experimentally the critical Reynolds number for the second, oscillatory bifurcation, Re_{co}^{exp}, for different bodies whose length-to-diameter ratio varied from $L/D = 1$ to $L/D = 6$. To determine the critical value of the Reynolds number, Re_{co}^{exp}, we examined the evolution with the Reynolds number of the squared amplitude of the streamwise velocity fluctuations, $w_{f_c}'^2$, defined here as (see Sanmiguel-Rojas *et al.* 2009)

$$w_{f_c}'^2 = \int_{f_c - \Delta f_d}^{f_c + \Delta f_u} PSD(f) \, \mathrm{d}f, \tag{3.1}$$

where $PSD(f)$ is the power spectral density obtained from the velocity measurements, f_c is the characteristic shedding frequency, and Δf_d and Δf_u correspond to the interval of frequency around f_c for which the power spectral density drops down to 5 % of the peak value. The linear increase of $w_{f_c}'^2$ with the Reynolds number near the critical value indicates that the transition to the oscillatory regime corresponds to a supercritical Hopf bifurcation. The critical value of the Reynolds number was then determined by linear regression of the experimental measurements of $w_{f_c}'^2$ near criticality. To quantify the experimental error and the independence of the critical Reynolds number of the downstream position at which the measurements were taken, we determined Re_{co}^{exp} at different axial positions. Thus, we obtained critical values of the Reynolds number at $z = 2, 3, 5$ and 7, finding discrepancies always smaller than 1 %. Special care was taken in our experiments to align the bodies under study with the free stream; however, a small misalignment could result in errors of the order of 5 %.

Figure 13(*a*) shows the dependence of the energy on the velocity fluctuations, $w_{f_c}'^2$, at $(r = 0, z = 3)$, with the Reynolds number near the critical point for bodies of aspect ratio $L/D = 1, 2, 3, 4$ and 6 respectively, indicating that Re_{co}^{exp} increases as L/D increases. Similarly, figure 13(*b*) displays the evolution with the Reynolds number of the energy of the tangential velocity perturbations at $(r = 0, z = 7)$ given by the numerical simulations for $L/D = 2$. Note that the prediction of the oscillatory
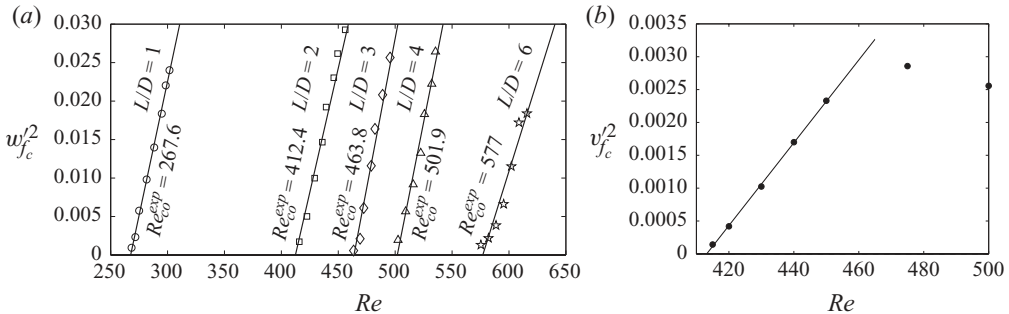
FIGURE 13. (*a*) Energy of the streamwise velocity fluctuations $w'^2_{f_c}$ obtained experimentally at $(r = 0, z = 3)$, as a function of the Reynolds number for the different bodies of $L/D = 1, 2, 3,$ 4 and 6 used in this work. (*b*) Energy of the tangential velocity perturbations, $v'^2_{f_c}$, at $(r = 0, z = 7)$ versus the Reynolds number given by the numerical simulations for a body of $L/D = 2$.

bifurcation given by the numerical simulations for a bullet-like body of aspect ratio equal to 2, $Re^{3d}_{co} \simeq 413$, is nearly identical to the experimental simulations, $Re^{exp}_{co} \simeq 412.4$, though the numerical result shows a deviation from the linear behaviour predicted by the Landau model at $Re > 450$ because of the developments of new frequencies discussed above. Similarly, the modes observed for the body aspect ratio $L/D = 1$ are the same as those found for $L/D = 2$, as described in Appendix B, and the critical Reynolds number obtained from the numerical simulations for a body of $L/D = 1$, $Re^{3d}_{co} \simeq 254$, agrees fairly well with the experimental value, $Re^{exp}_{co} \simeq 267.6$. Since this second transition is also due to a reflectional symmetry-preserving mode, there are marked differences in the phenomenology of the hemielliptic geometry considered in this work with respect to the hemisphere, which exhibits a second reflectional symmetry-breaking mode (Kim & Choi 2003). The relative difference between the critical values of the Reynolds number associated with the SS and RSP modes obtained from the numerical simulations, Δ^{3d}, is larger than 0.18 for $L/D \geqslant 1$. Consequently, the assumption of simultaneously nearly neutral modes, e.g. Fabre *et al.* (2008), is questionable for afterbodies, as we further discuss below.

The same qualitative behaviour has been observed as the body aspect ratio, L/D, is modified. Figure 14 shows the effect of L/D on the critical Reynolds numbers, without base bleed, obtained from our experimental measurements, numerical simulations and global linear stability for $|m| = 1$. It can be observed that, in the particular case of $L/D = 1$ and 2, the critical Reynolds number for the first, steady bifurcation given by the global linear stability analysis agrees very well with that obtained from the numerical simulations, $Re^{GLS}_{cs} \simeq Re^{3d}_{cs}$ (numerical simulations for larger bodies, $L/D > 2$, were not performed). Furthermore, as mentioned above, the predictions of the critical Reynolds number for the second, oscillatory bifurcation obtained numerically also agree with the experimental results, $Re^{3d}_{co} \simeq Re^{exp}_{co}$; however, the global stability analysis considerably overestimates the critical Reynolds number associated with the oscillatory bifurcation. Thus, the value of $\Delta^{GLS} = (Re^{GLS}_{co} - Re^{GLS}_{cs})/Re^{GLS}_{cs}$, based on the global linear stability analysis, varies from 0.29 for $L/D = 1$ to 1.04 for $L/D = 10$, indicating that the effect of considering an unperturbed base flow on the stability analysis induces larger errors in the prediction of Re_{co} and St as L/D increases. Indeed, the relative gap between the critical Reynolds numbers for the sphere is nearly equal to that of our hemi-ellipse, but the global linear stability analysis works much better for the sphere (Pier 2008). Consequently, it is expected
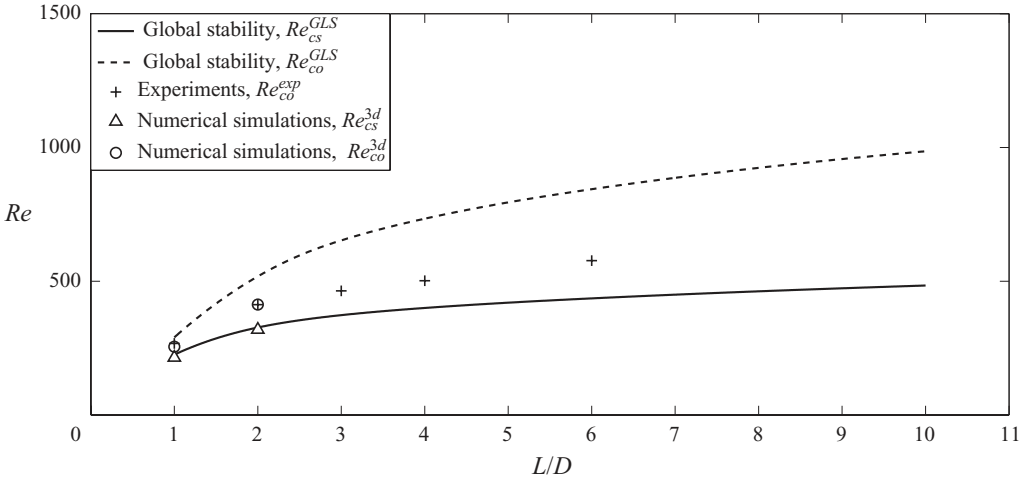
FIGURE 14. Dependence of the critical Reynolds numbers on the aspect ratio of the body, L/D, for the case without base bleed, $C_b = 0$. Comparison among the results given by the linear global stability analysis (superscript GLS), numerical simulations for $L/D = 1, 2$ (superscript $3d$) and experiments for $L/D = 1, 2, 3, 4$ and 6 (superscript exp). Note that the subscripts cs and co denote the critical Reynolds number for the onset of the steady and oscillatory modes, respectively.

that the saturated amplitude of the mode yielding the transition to the SS state is much larger for the geometries analysed herein than for the sphere. It is worth mentioning that Δ also increases with the Mach number for an afterbody (see Meliga, Sipp & Chomaz 2010a; Meliga *et al.* 2010b), and thus the theoretical quantification of the reflectional symmetry-preserving mode in the compressible regime may also deserve the use of either three-dimensional global stability analysis (Bagheri *et al.* 2009) or three-dimensional numerical simulations. Figure 14 also shows that, as L/D increases, the critical Reynolds number increases for both modes, indicating that the wake is more stable for longer bodies.

3.2. *Description of the flow field and results with base bleed, $C_b > 0$*

Several works have demonstrated that the presence of base bleed has a strong stabilizing effect on two-dimensional bluff-body wakes (see for instance Wood 1964, 1967; Bearman 1967; Schumm, Berger & Monkewitz 1994; Hammond & Redekopp 1997; Arkas & Redekopp 2004). In the particular case of blunt-based axisymmetric bodies, of interest in this work, Sevilla & Martínez-Bazán (2004) showed that the large-scale helical structures present in the high-Reynolds-number turbulent wake can be inhibited by means of a sufficiently large value of the base bleed coefficient, in agreement with corresponding local stability calculations. Similarly, in the case of the laminar wake which prevails at moderately large values of the Reynolds number, the global stability analysis performed by Sanmiguel-Rojas *et al.* (2009) showed the existence of critical values of the bleed coefficient to stabilize both the steady and subsequent oscillatory global modes appearing in the steady axisymmetric wake. Note that both the local and global linear stability analyses respectively performed in Sevilla & Martínez-Bazán (2004) and Sanmiguel-Rojas *et al.* (2009) consider the steady axisymmetric wake as basic flow, an approximation also used in the present work. Moreover, base bleed control of unsteadiness in a compressible afterbody wake has recently been investigated by Meliga *et al.* (2010b) through a global linear stability
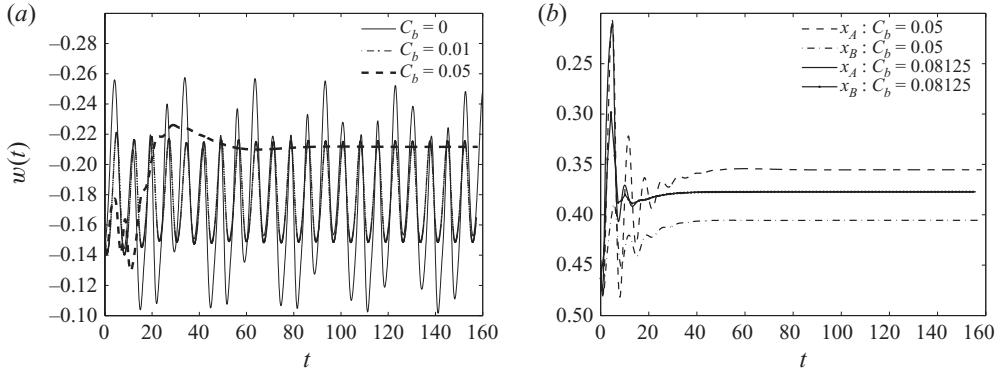
FIGURE 15. Time series of the streamwise velocity, $w(t)$, obtained numerically at (*a*) ($r = 0$, $z = 1$) for the values of the bleed coefficient $C_b = 0$, 0.01 and 0.05, and (*b*) at $x_A \equiv (0.5, 0, 1)$ and $x_B \equiv (0.5, \pi/2, 1)$ for $C_b = 0.05$ and 0.08125. Here, $Re = 500$.

analysis of the basic axisymmetric state. However, as already discussed in §3.1, the wake is not axisymmetric at the onset of unsteadiness due to the symmetry-breaking mode which bifurcates at smaller values of the Reynolds number, leading to linear stability predictions for the critical Reynolds number which are quantitatively wrong. Since this is also expected to affect to the corresponding values of the critical bleed coefficients, in this section we will present results obtained not only through local and global stability analyses but also from direct numerical simulations of the wake with base bleed, as well as experimental measurements.

Let us show first the results obtained from the numerical simulations performed for a body of aspect ratio $L/D = 2$ at a Reynolds number of 500, for which the wake is unsteady as discussed in §3.1. The fluctuations of streamwise velocity, $w(t)$, at the particular location ($r = 0$, $z = 1$), are displayed in figure 15(*a*) for several values of the bleed coefficient, namely $C_b = 0$, 0.01 and 0.05, clearly illustrating the stabilizing effect of base bleed on the oscillatory mode. Note from figure 15(*a*) that, in the case without base bleed, $C_b = 0$ (solid line), the velocity signal is multimodal and indicates the presence of a low-frequency mode as discussed in §3.1 (see figure 11). However, the introduction of a very small amount of base bleed, $C_b = 0.01$ (dash-dotted line), makes the velocity signal perfectly monochromatic after a short relaxation time of the order of one shedding period, accompanied by a slight reduction in the oscillation amplitude. It is interesting to note that this unimodal behaviour is similar to that observed without base bleed at values of the Reynolds numbers closer to the critical one. It is also observed in figure 15(*a*) that for a base bleed coefficient of $C_b = 0.05$ (dashed line), the centreline velocity signal reaches a constant value after relaxation, indicating a complete suppression of the oscillatory mode. Clearly, there exists a critical value of the bleed coefficient $0.01 < C_{b2}^* < 0.05$ such that the oscillatory global mode is inhibited for values of $C_b > C_{b2}^*$. Unfortunately, the three-dimensional unsteady numerical simulations are especially time-consuming close to criticality, thus making the accurate determination of the curve $C_{b2}^*(Re)$ a difficult task to deal with. Consequently, only upper and lower bounds have been obtained for the values of C_{b2}^* at different Reynolds numbers, as discussed below.

A more detailed study reveals that for $C_b = 0.05$, while the unsteady mode is completely suppressed at $Re = 500$, the steady symmetric mode still persists. This fact is illustrated in figure 15(*b*), where the streamwise velocity is plotted versus time,

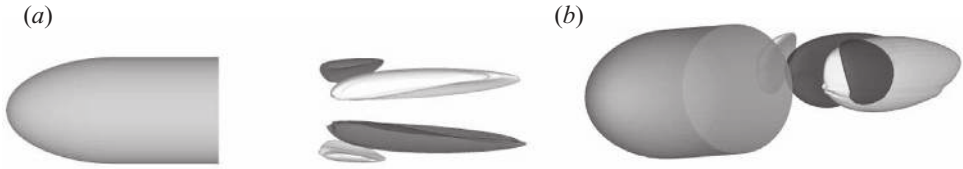(a)   (b)

FIGURE 16. Isosurfaces of the streamwise vorticity, $\omega_z = \pm 0.05$, for $Re = 1000$ and $C_b = 0.105$: (a) plan and (b) perspective views. The flow is steady and exhibits planar symmetry.

during the transients following the imposition of a constant base bleed coefficient $C_b = 0.05$, at the points x_A and x_B, with (r, θ, z) coordinates respectively given by $(0.5, 0, 1)$ (dashed line) and $(0.5, \pi/2, 1)$ (dash-dotted line). Taking into account that the points x_A and x_B are located at positions differing only by a 90° azimuthal rotation, the fact that their corresponding asymptotic, axial steady velocities are different, $w(x_A) \simeq 0.35$, $w(x_B) \simeq 0.4$, indicates the absence of axisymmetry in the wake for $Re = 500$ and $C_b = 0.05$. Nevertheless, the axisymmetric state can be recovered at $Re = 500$ by increasing the base bleed coefficient past a certain critical value given by $C_{b1}^* \simeq 0.0723$, as explained in more detail in Appendix B. For instance, in figure 15(b) it can be seen that the steady streamwise velocities are identical at the points x_A and x_B for a bleed coefficient of $C_b = 0.08125$.

The critical bleed coefficient $C_{b1}^*(Re)$ needed to restabilise the steady-state mode increases with the Reynolds number giving, for instance, a value $C_{b1}^* \simeq 0.11$ for $Re = 1000$. Consequently, the steady non-axisymmetric wake can exhibit a considerable downstream displacement for $C_b < C_{b1}^*$, specially at large Reynolds numbers. This feature is illustrated in figure 16, where the isocontours of streamwise vorticity $\omega_z = \pm 0.05$ are shown for $Re = 1000$ and $C_b = 0.105$, slightly below C_{b1}^*. It can be clearly seen that the axisymmetry-breaking mode is present, as revealed by the existence of a symmetry plane, while, at the same time, the vortical structures present in the double-threaded wake are located at a considerable distance downstream of the body base due to the effect of the base bleed momentum. The procedure followed to determine C_{b1}^* and its dependence on the Reynolds number is similar to that employed in the computation of $Re_{cs}^{3d}(L/D)$ in the case without base bleed, as described in Appendix B.

In addition to looking for critical values of the base bleed coefficient, we have also performed a more detailed numerical study of its effect on the unsteady wake in the nonlinear regime at several values of $C_b < C_{b2}^*(Re)$, for which the oscillatory mode is self-excited with a finite amplitude. As an example, figure 17 shows the power spectral density of the streamwise velocity component at $z = 7$, as a function of the Strouhal number, St, for a body with $L/D = 2$, at a Reynolds number of $Re = 430$. This figure reveals the presence of a single peak in the spectrum, corresponding to the periodic and monochromatic shedding of vortices in the wake at $Re = 430$. Note from figure 17 that the injection of a very small base-bleed flow rate with $C_b = 0.005$ (solid line) decreases the amplitude of the peak from $\simeq 0.1$ in the case without base bleed (dashed line) to $\lesssim 0.01$ for $C_b = 0.005$. Note also that the value of the Strouhal number, $St \simeq 0.128$, is hardly affected by C_b at this particular Reynolds number, $Re = 430$. More generally, both experiments and numerical simulations showed that the Strouhal number has a very weak dependence on C_b, but increases with Re at a given value of C_b, as can be observed in figure 20. At higher Reynolds numbers where, in the case without base bleed, the velocity signal is multimodal, the addition
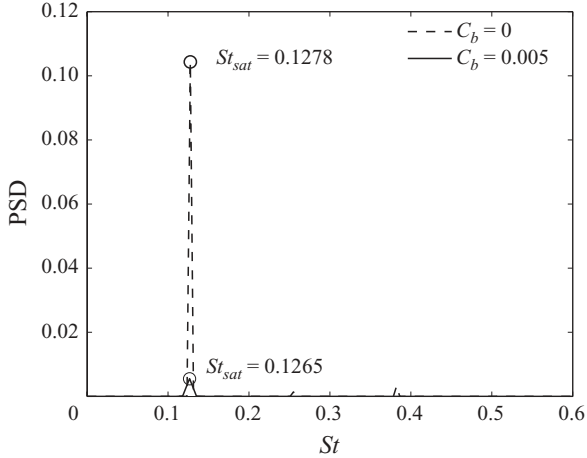
FIGURE 17. Power spectral density of the streamwise velocity component at $(r=0, z=7)$ for a body of aspect ratio $L/D = 2$, at a Reynolds number of $Re = 430$ and $C_b = (0, 0.005)$.

of base bleed first makes the velocity fluctuations monochromatic and, for larger values of C_b, completely stabilises the wake.

The effect of base bleed on the eigenvalue spectra of linear global modes has been discussed in detail in Sanmiguel-Rojas *et al.* (2009). For the particular case of a body with $L/D = 2$, the corresponding results are summarised in figure 18, where the eigenvalues (σ_r, σ_i) are plotted for $Re = 500$, $|m| = 1$, and four different values of $C_b = (0, 0.04, 0.06, 0.08)$. Note from figure 18 that as C_b increases, the leading eigenvalues σ^s and σ^o, corresponding respectively to the steady and oscillatory modes, move towards the stable $\sigma_r < 0$ half-plane. Specifically, figure 18(*a*) shows that for $C_b = 0$, the oscillatory mode is slightly damped, in agreement with the fact that $Re_{co}^{GLS} = 518$ in this case (see figure 8), and has an associated frequency $\sigma_i^o \simeq 0.65$. However, it is also observed in figure 18(*a*) that, since $Re_{cs}^{GLS} = 327$ (see figure 14), the steady-state mode is unstable, $\sigma_r^s > 0$ without base bleed. Figure 18(*b–d*) reveals that both growth rates σ_r^s and σ_r^o decrease as C_b increases and, in particular, figures 18(*c*) and 18(*d*) show that $0.06 < C_{b1}^* < 0.08$. More generally, for given values of L/D, Re and C_b, the conditions $\sigma_r^s = 0$ and $\sigma_r^o = 0$ were used to determine the critical bleed coefficients C_{b1}^* and C_{b2}^*, respectively.

Figure 19 summarises the values of the critical base-bleed coefficients obtained using local (crossed line) and global (solid and dashed lines) stability analyses, as well as those computed by means of direct numerical simulations performed for $Re = (430, 450, 500, 600, 800)$ (circles and triangles) and, in the case of the steady bifurcation, also $Re = 1000$ (circle). Similar to the case of Re_{cs}^{3d} discussed above, a perfect agreement is obtained between the direct numerical simulations and global stability predictions for the curve $C_{b1}^*(Re)$ (circles and solid line, respectively), demonstrating the capability and accuracy of the global stability approach in this case. The accurate determination of $C_{b1}^*(Re)$ by the global stability analysis is of practical interest because it allows us to quantify the upper bound for the bleed coefficient required to inhibit not only the steady mode but also the periodic state, at least for the parameter settings investigated here. Therefore, since the direct numerical simulations are much more time-consuming than the global stability analysis, they were only used to compute the $C_{b1}^*(Re)$ neutral curve for values of the Reynolds number $Re \leqslant 1000$, the remaining range $1000 \leqslant Re \leqslant 2000$ being covered only by the results obtained
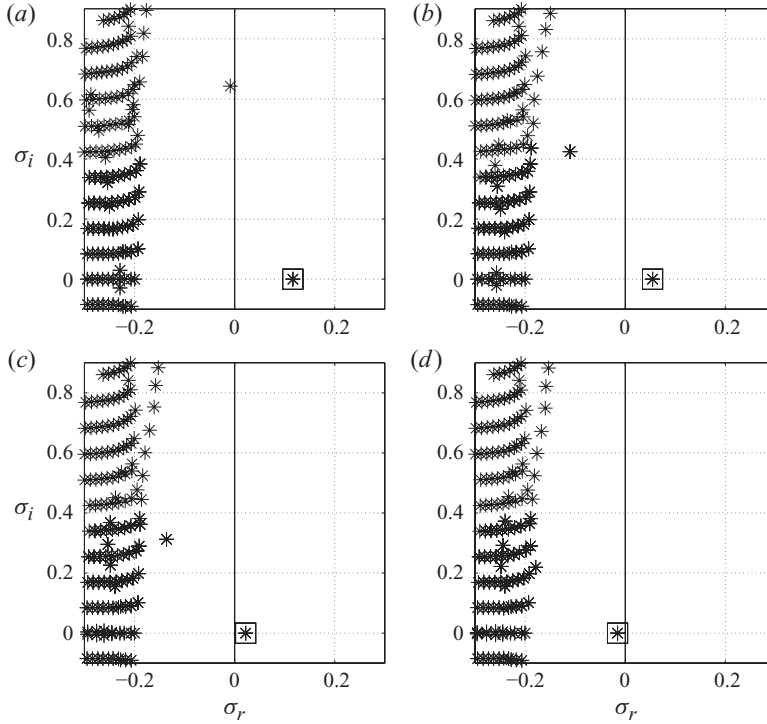
FIGURE 18. Eigenvalue spectra for a body with aspect ratio $L/D = 2$, $Re = 500$, $|m| = 1$ and base bleed coefficients (a) $C_b = 0$, (b) $C_b = 0.040$, (c) $C_b = 0.060$ and (d) $C_b = 0.080$, respectively. The unstable eigenvalue corresponding to the steady bifurcation has been marked with a square.

through the global stability analysis. Note that the condition $C_b > C_{b1}^*(Re)$ defines a region of the (Re, C_b) parameter plane, referred to as region I in figure 19, within which the wake subjected to base bleed is steady and axisymmetric. Figure 19 also shows that the trend of the curve $C_{b1}^*(Re)$ is consistent with the existence of an asymptote at large Reynolds numbers, such that $C_{b1}^* \rightarrow 0.125$ for $Re \rightarrow \infty$. However, this result must be interpreted with care, since the instability of the shear layer separating from the body base may induce the transition to turbulence in the wake for large enough values of the Reynolds number (see for instance Prasad & Williamson 1997).

For values of C_b such that $C_{b2}^*(Re) < C_b < C_{b1}^*(Re)$, defined as region II in figure 19, the wake is steady and exhibits planar symmetry, having in this case a near field similar to that shown in figure 16. However, when the bleed coefficient is decreased below the critical value C_{b2}^*, i.e. for $C_b < C_{b2}^*(Re)$, the oscillatory mode is destabilised, corresponding to region III in figure 19. In this case, periodic vortex shedding of vortex structures takes place, resembling the cases displayed in figures 6 and 7 for the case without base bleed.

Furthermore, as revealed by figure 19, the critical values $C_{b2}^*(Re)$ computed with the local and global stability analyses, respectively shown as crossed and dashed lines, are in good agreement for large enough values of the Reynolds number, $Re \gtrsim 1200$. This result can be explained by noting that the slenderness of the basic flow at criticality increases with C_b, as already pointed out in Sevilla & Martínez-Bazán (2004), thereby justifying the use of the quasi-parallel approximation. However, for Reynolds number $Re \lesssim 800$, the global stability analysis predicts values of C_{b2}^* considerably smaller
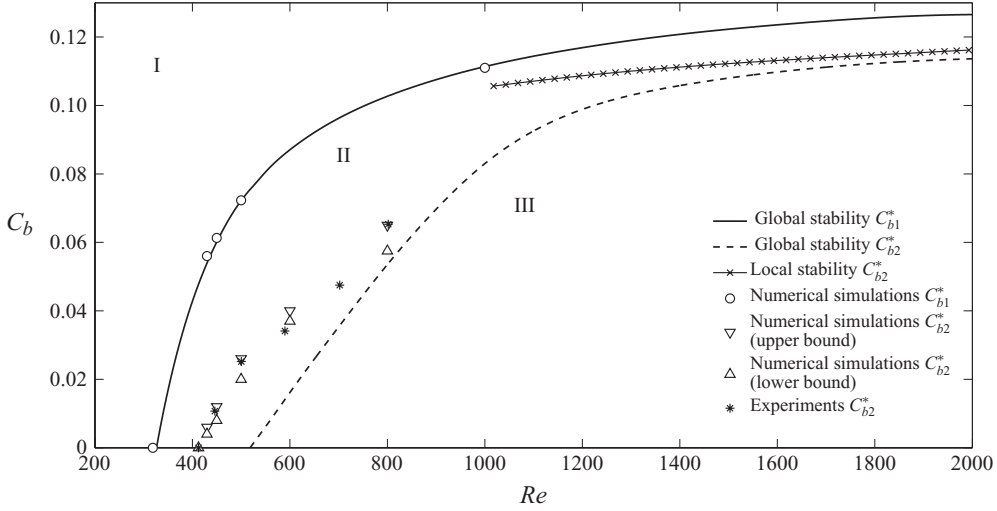
FIGURE 19. Evolution of the critical base bleed coefficients with the Reynolds number for an ellipsoidal rounded nose body of aspect ratio $L/D = 2$. The results of the local and global linear stability analyses correspond to the most unstable azimuthal mode, $|m| = 1$. Solid and dashed lines represent the critical bleed coefficients needed to stabilize the stationary, C_{b1}^*, and oscillatory, C_{b2}^*, global modes, respectively, computed from the linear global analysis, while the line with crosses displays the value of C_{b2}^* resulting from the local analysis. Circles ($\circ$) indicate the evolution of C_{b1}^* with the Reynolds number obtained from the numerical simulations following the methodology discussed in Appendix B, and $\triangledown$ and $\triangle$ display the upper and lower bounds on C_{b2}^* determined by the simulations. The experimental values of C_{b2}^* are depicted by $*$.

than those obtained through experiments and direct numerical simulations, which clearly cannot be used to obtain the critical bleed coefficient in that region. As the Reynolds number decreases, the value of C_{b2}^* given by the global analysis decreases for $Re \lesssim 800$, until it becomes zero at $Re = Re_{co}^{GLS} \simeq 518$. The quantitative disagreement obtained between Re_{co}^{3d} and Re_{co}^{GLS}, respectively computed through direct numerical simulations and global linear stability analysis, corresponds in figure 19 to the different intersection points observed in both cases at $C_b = 0$. Accordingly, in the case with base bleed, both approaches lead to different values of $C_{b2}^*(Re)$, such that the lower limit of the critical bleed coefficient predicted by the direct numerical simulation (up triangles) are larger than those given by the global analysis (dashed line) for values of the Reynolds number $Re \lesssim 800$, indicating that, at these Reynolds numbers, the planar-symmetric wake is more unstable than the axisymmetric wake used as base flow in the linear stability analysis. Nevertheless, note that the difference between the values of $C_{b2}^*(Re)$ obtained from the numerical simulations and the linear analysis decreases as Re increases, with a fairly good agreement at $Re = 800$. Figure 19 also indicates that, similar to the case of the critical bleed coefficient C_{b1}^*, the values of C_{b2}^* obtained from the local and global analyses tend to a common asymptotic value such that $C_{b2}^* \rightarrow 0.115$, approximately, for $Re \rightarrow \infty$ and in the particular case of a body with $L/D = 2$. Unfortunately, due to computational limitations, we were not able to perform accurate unsteady numerical simulations for $Re > 800$ with the aim of obtaining the corresponding values of C_{b2}^*.

The experimental results for C_{b2}^*, plotted with asterisks in figure 19, are in good agreement with the corresponding values given by the numerical simulations
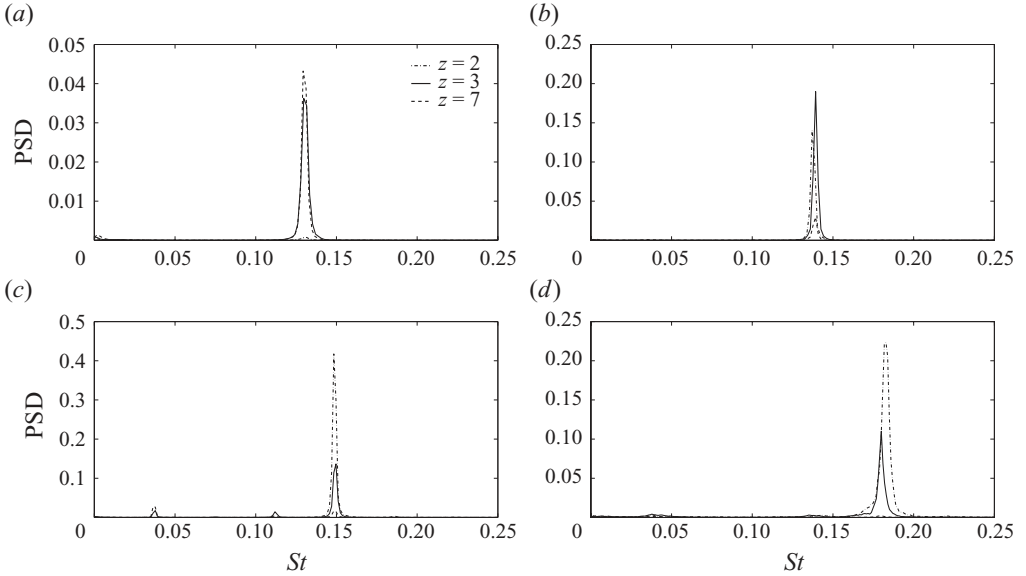
FIGURE 20. Power spectral density of the streamwise velocity component as a function of St, measured experimentally for $C_b = 0$ at (a) $Re = 446$, (b) $Re = 500$, (c) $Re = 590$ and (d) $Re = 802$, illustrating the downstream dependence of the oscillatory mode amplitude.

(triangles). These experimental results were obtained taking into account the fact that the maximum amplitude of the streamwise velocity fluctuations occurs at a downstream position which depends on the value of Re. As an example, figure 20 shows the power spectral densities of the streamwise velocity as a function of St for $C_b = 0$ and $Re = (446, 500, 590, 802)$, measured at $r = 0$ and three different downstream positions $z = (2, 3, 7)$ (dash-dotted, solid and dashed lines, respectively). As shown by figure 20(a), for a value of $Re = 446$, close to criticality, the intensity of the oscillating mode is very small at $z = 2$ (dash-dotted line), but increases downstream to reach values which are similar at $z = 3$ and $z = 7$ (solid and dashed lines, respectively). However, at a slightly larger value of $Re = 500$ figure 20(b) indicates that the amplitude is maximum at $z = 3$ and that at $z = 7$ the energy around the peak has decayed considerably. As the Reynolds number increases, the most intense oscillations take place at decreasing values of z; thus, figures 20(c) and 20(d) show that the largest oscillation amplitudes are obtained at $z = 2$ both for $Re = 590$ and $Re = 802$. It is worth mentioning that these experimental observations were consistent with the numerical simulations, although the corresponding results are not shown for conciseness. Moreover, the results of figure 20 clearly show how the dominant Strouhal number increases with Re.

The procedure followed to obtain the experimental values of C_{b2}^* shown in figure 19 can be summarised as follows. For a fixed value of Re, the hot-wire probe was located at the downstream position of maximum oscillation amplitude in the absence of base bleed, discussed in the previous paragraph, and the streamwise velocity signal was then recorded for several values of C_b. As an example, figure 21(a) shows the power spectral densities obtained at $Re = 500$ and $C_b = (0, 0.018, 0.023, 0.026)$. In this case, the measurements were performed at $z = 3$, following the maximum-energy criterion introduced above. The spectra represented in figure 21(a) reveal the strong stabilising effect of base bleed: a relatively small value of $C_b = 0.018$ provides a nearly
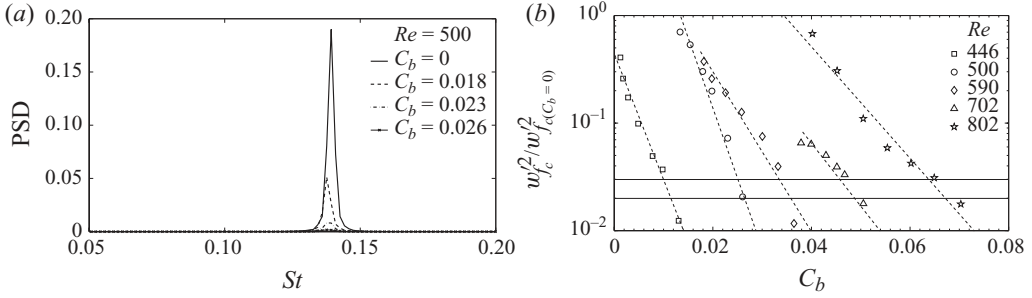
FIGURE 21. (*a*) Evolution of the PSD of the streamwise velocity component with the bleed coefficient obtained experimentally at $z = 3$ and $Re = 500$. (*b*) Energy of the streamwise velocity fluctuations $w_{f_c}'^2/w_{f_c(C_b = 0)}'^2$ versus the bleed coefficient for different Reynolds numbers obtained experimentally at the most energetic position.

fourfold decrease in the amplitude of the spectral peak with respect to the case without base bleed, $C_b = 0$, without introducing significant changes in its width. This stabilising effect persists for increasing values of C_b, as illustrated in figure 21(*a*) for the particular cases of $C_b = 0.023$ and 0.026. To quantify the stabilization process associated with increasing C_b at a fixed value of Re, as well as to obtain the corresponding critical values of $C_{b2}^*(Re)$, we decided to follow a procedure similar to that used by Schumm *et al.* (1994); the saturated oscillation amplitude, normalised with the value without base bleed, $w_{f_c}'^2/w_{f_c(C_b = 0)}'^2$, is plotted in figure 21(*b*) as a function of C_b for several values of Re indicated in the legend. The results of figure 21(*b*), which are qualitatively similar to those shown in figure 18(*a*) of Schumm *et al.* (1994) for the wake of a two-dimensional blunt-based body, demonstrate the stabilising effect of base bleed on a wide range of values of Re. Moreover, it can be observed in figure 21(*b*) that the values of C_b needed to achieve a given value of the normalised oscillation energy increase with Re. Unfortunately, the function $w_{f_c}'^2/w_{f_c(C_b = 0)}'^2(C_b)$ obtained from these experiments was not linear near criticality, as expected in the case of a Hopf bifurcation in terms of C_b, but showed exponential-like behaviour. Therefore, it seems that the result by Hannemann & Oertel (1989, figures 20 and 23) does not apply at all Re (see below). This fact, which can also be inferred from the results shown in figure 18(*a*) of Schumm *et al.* (1994), precluded us from performing a linear regression in the neighbourhood of the bifurcation point to determine the function $C_{b2}^*(Re)$. Instead, the critical values C_{b2}^* plotted in figure 19 were obtained by applying an exponential fit to the tail of the $w_{f_c}'^2/w_{f_c(C_b = 0)}'^2(C_b)$ experimental curve, as shown by dashed lines in figure 21(*b*). The value of C_{b2}^* was then obtained by the condition $w_{f_c}'^2/w_{f_c(C_b = 0)}'^2(C_{b2}^*) = \epsilon \ll 1$. Although the value of the marginal amplitude $\epsilon = 0.03$ (3 %) was chosen arbitrarily, it can be seen in figure 21(*b*) that the value of C_{b2}^* is not very sensitive to its specific value, as illustrated by the solid horizontal lines plotted in figure 21(*b*) for the particular cases $\epsilon = 0.02$ (2 %) and $\epsilon = 0.03$ (3 %).

It is noteworthy that the marginal curve $C_{b2}^*(Re)$ has a structure similar to that found by Schumm *et al.* (1994) in the case of a two-dimensional blunt-based geometry (see their figure 18*b*), which allows us to question the assumption of a dual Hopf bifurcation in terms of both C_b (with $Re = $ constant) and Re (with $C_b = $ constant). A possible explanation can be given as follows. If, at constant Re, there was a Hopf bifurcation in terms of C_b, one could state that $w_{f_c}'^2 \propto (C_{b2}^*(Re) - C_b)$. Thus, a linear dependence of $w_{f_c}'^2$ with Re should only be observed in a region where the neutral

curve behaved as $C_{b2}^*(Re) \propto Re$. However, figure 19 illustrates that $C_{b2}^*(Re)$ is not a linear function of Re, indicating that the second, oscillatory bifurcation might not correspond to a supercritical Hopf bifurcation in terms of C_b when the Reynolds number is kept constant.

4. Conclusions

Experiments, numerical simulations and linear stability analysis have been used to perform a detailed study of the laminar wake behind a slender axisymmetric body with a 2:1 ellipsoidal nose and a blunt trailing edge at zero angle of attack. Our work focuses on the instabilities taking place in the flow for increasing values of the Reynolds number up to $Re = 2000$, considering also the effect of the body length-to-diameter ratio in the range $1 \leqslant L/D \leqslant 10$. The injection of ambient fluid through the body base, commonly referred to as base bleed, was also studied as a simple method to inhibit the instabilities of the wake.

For increasing Reynolds numbers, both the three-dimensional numerical simulations and the global stability analysis predict the existence of a first steady axisymmetry-breaking bifurcation, as is known to happen in the case of other axisymmetric bodies like spheres or disks. We show that this steady bifurcation takes place at a critical value of the Reynolds number, $Re_{cs}(L/D)$, which slightly increases with the aspect ratio of the body. The values computed from the numerical simulations and the stability analysis, Re_{cs}^{3d} and Re_{cs}^{GLS}, respectively, are in very good quantitative agreement for the two particular cases considered in the numerical simulations, namely $L/D = 1$ and 2. In the particular case of a body with $L/D = 2$, the corresponding values are given by $Re_{cs}^{3d} \simeq 319$ and $Re_{cs}^{GLS} \simeq 327$. Similar to the cases of the sphere and the disk, the structure of the steady wake prevailing for $Re > Re_{cs}(L/D)$ is planar-symmetric and features a double-threaded structure consisting of a pair of counter-rotating streamwise vortices oriented at an angle with respect to the symmetry axis of the body. A second oscillatory bifurcation has been shown to exist at a higher value of the Reynolds number, Re_{co}, whose values are given by Re_{co}^{exp}, Re_{co}^{3d} and Re_{co}^{GLS} according to experiments, numerical simulations and global stability analysis, respectively, all of which increase with L/D. The numerical simulations revealed that, as happens in the case of a sphere, the symmetry plane which appears in the wake at $Re = Re_{cs}$, is preserved for $Re > Re_{co}$, and is thus a symmetry-preserving mode according to Fabre *et al.* (2008). Experiments and numerical simulations are in good quantitative agreement in all the cases considered, $Re_{co}^{exp} \simeq Re_{co}^{3d}$, providing further validation for the numerical code. In the case with $L/D = 2$, the critical Reynolds numbers were found to be $Re_{co}^{exp} \simeq 412.4$ and $Re_{co}^{3d} \simeq 413$, while, for $L/D = 1$, $Re_{co}^{exp} \simeq 267.6$ and $Re_{co}^{3d} \simeq 254$. However, the global linear stability analysis predicts an oscillatory bifurcation for a Reynolds number which is significantly higher than that predicted by the experiments and the numerical simulations, giving for instance $Re_{co}^{GLS} \simeq 518$ for $L/D = 2$. The errors in the predictions made by the global stability analysis for the critical Reynolds number associated with the oscillatory bifurcation are due to the use of an axisymmetric basic flow for Reynolds numbers higher than that corresponding to the first bifurcation. This error is substantially larger for the bullet-like geometry considered in the present work than in the cases of a sphere and a thin disk studied by Pier (2008) and Fabre *et al.* (2008). In the particular case of the wake of a thin disk, a natural explanation for the relatively small error in the value of Re_{co} predicted by the global linear stability analysis applied to the axisymmetric base flow is the fact that the relative gap in the critical Reynolds

numbers, $\Delta^{GLS} = (Re_{co}^{GLS} - Re_{cs}^{GLS})/Re_{cs}^{GLS} \ll 1$ (Fabre *et al.* 2008). However, since the values of Δ^{GLS} are similar in the cases of the sphere (Pier 2008) and the hemiellipse considered in this work, this argument alone cannot explain the smaller relative error obtained for the sphere. Therefore, we are led to the conclusion that, as suggested by an anonymous referee, the saturated amplitude of the steady-state mode evaluated at the critical Reynolds number corresponding to the onset of the oscillating mode, Re_{co}, must be smaller for the sphere than for the bullet-like geometry. However, this hypothesis clearly deserves further study and is left for a future work. The difference $(Re_{co}^{GLS} - Re_{co}^{exp})$ has been found to increase with the aspect ratio of the body, L/D. These results imply, in particular, that care must be taken when studying the oscillatory regimes of afterbody wakes, specially for large aspect ratio geometries. Even though the relative quantitative errors involved in using axisymmetric base states in global stability analyses have been shown to be high in these cases, this approach has been routinely used in recent works (see for instance Meliga *et al.* 2010a,b). In addition, the results reported in the present work may also serve as a benchmark for more involved three-dimensional linear stability analyses (see for example Pier 2008; Bagheri *et al.* 2009).

The three-dimensional numerical simulations performed in this work have revealed the existence of remarkable differences between the wakes of slender blunt-based bodies and other previously studied geometries such as the sphere, hemisphere or disk. First, it is noteworthy that the symmetry plane which appears in the wake after the first steady bifurcation is preserved for Reynolds numbers up to $Re = 500$, even in the presence of strong nonlinear interactions of the shed vortical structures, and subsequent harmonic generation. In contrast, although wakes of other objects like spheres and disks also present an RSP regime, the corresponding range of Reynolds numbers is much narrower. In addition, for $Re \gtrsim 500$, we have found the existence of a new regime in which the wake interacts with the boundary layer on the solid body, inducing a periodic oscillation with a frequency of about one-quarter of the leading one. Bouchet *et al.* (2006) also reported the existence of a Hopf bifurcation accompanied by the onset of a second oscillation frequency on the wake of a sphere at $Re \sim 325$ and a similar regime, denoted 'Honky-Tonky' mode, has recently been reported in the wake of a thick disk by Auguste *et al.* (2010) for $Re \gtrsim 217$, where the lowest frequency is given by approximately one-third of the leading one. However, in the case of a thick disk, this flow regime, characterized by the presence of a secondary low frequency while preserving the reflectional symmetry, appears after a sequence of flow bifurcations not found in the configuration under study in this work.

Base bleed has been found to stabilize the wake in the range of Reynolds numbers considered in this work. More specifically, the parameter plane (Re, C_b), spanned by the Reynolds number and the bleed coefficient, defined here as the bleed to ambient velocity ratio, can be divided into three different regions, as shown in figure 19 for the particular case of a body with $L/D = 2$. In region I, where $C_b > C_{b1}^*(Re)$, the wake is steady and axisymmetric, and thus completely restabilised due to the effect of the base bleed. In region II, defined by $C_{b2}^*(Re) < C_b < C_{b1}^*(Re)$, the wake is steady and planar-symmetric, with a structure similar to that found for $Re_{cs} < Re < Re_{co}$ in the case without base bleed, $C_b = 0$. Finally, in region III, in which $C_b < C_{b2}^*(Re)$, periodic shedding of vortices takes place due to the excitation of the oscillatory mode. The global stability analysis predicts that the critical bleed coefficients tend to asymptotic values $C_{b1}^* \to 0.125$ and $C_{b2}^* \to 0.115$ for $Re \gtrsim 2000$, the latter also being in good agreement with results obtained with a local stability analysis of the axisymmetric base flow. The experiments performed in the case with base bleed showed good agreement
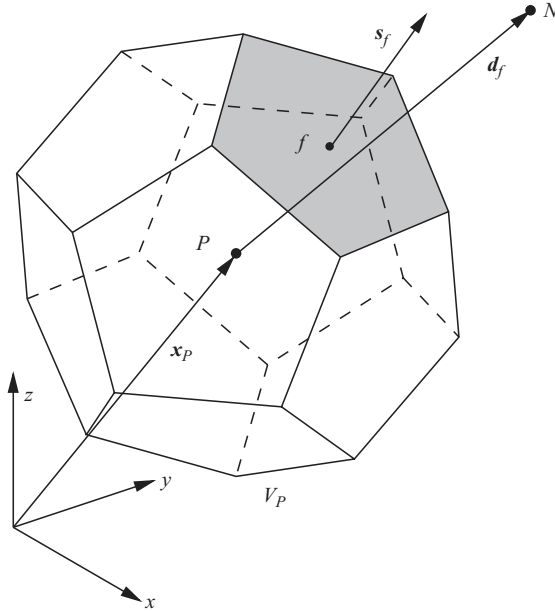
FIGURE 22. Example of a generic computational cell.

with the results obtained from the numerical simulations, giving similar values of $C_{b2}^*(Re)$ in the range of Reynolds numbers considered, $Re \lesssim 800$. It should be noted that the critical curve $C_{b1}^*(Re)$, which can be precisely predicted by means of a global stability analysis with an axisymmetric base flow, is enough to ensure a completely re-stabilised wake for $C_b > C_{b1}^*(Re)$ in the range of Reynolds numbers reported here. Moreover, its computational cost is much smaller than the fully three-dimensional numerical simulations that would be alternatively needed.

Let us finally emphasize that the shear layer separating from the body will induce the transition to turbulence in the wake for sufficiently large values of the Reynolds number, a regime which should be addressed in detail in a future work.

Supplementary movies are available at journals.cambridge.org/flm.

Appendix A. Numerical methods
A.1. *Numerical schemes implemented by OpenFOAM®*

OpenFOAM® discretizes (2.1) and (2.2) using the finite volume method (see Ferziger & Perić 2002). The starting point of the finite volume method is the mass and momentum conservation equations in their integral form, which are readily obtained after integrating (2.1) and (2.2) in a control volume (see figure 22, where the cell volume is denoted by V_P). All these equations are said to be in *strong conservation form* because all the terms are expressed in the form of the divergence of a vector or

tensor. The use of the strong conservation form of the equations, together with the finite volume method, automatically ensures global conservation. In fact, to preserve this property in the numerical solution, a fixed direction coordinate system (i.e. Cartesian components) was adopted in this work, although, for notational clarity and for the sake of coherence with §§ A.2 and A.3, the results are presented in cylindrical coordinates.

Furthermore, unknown dependent variables to be computed were stored at the cell centroid x_P, using thus the so-called collocated arrangement, $\int_{V_P} (x - x_P) \, dV = 0$. The main advantage of this approach is the reliability of handling complicated solution domains, as the one considered here. However, to overcome the main disadvantage of the collocated arrangement, that is, the occurrence of oscillations in the pressure field, an oscillation-free pressure–velocity coupling method in line with Rhie & Chow (1983) is adopted.

Figure 22 shows an example of the convex polyhedral cells supported by the solver, whose boundaries are composed of a set of convex polygons, although in the present work we use hexahedral cells. Each cell has a neighbouring cell across each of its faces, of centroid denoted by N, and positional vector relative to x_P for the face f defined as $d_f = x_N - x_P$. Similarly, using the centroid rule, the face centre, x_f, is given by $\int_{S_f} (x - x_f) \, dS = 0$. Next, the face area vector s_f is a surface normal vector whose magnitude is equal to the area of the face. The surface is numerically never flat, so the face area is calculated from the integrals $s_f = \int_{S_f} n \, dS$. In order to avoid non-orthogonal corrections during each time step of the numerical simulation, which are handled explicitly by OpenFOAM and increase proportionally the computational cost (Jasak 1996), we employed hexahedral cells with a mesh non-orthogonality average of, approximately, $4°$. Thus, the positional vector d_f is nearly parallel to the face area vector s_f, and non-orthogonal corrections do not improve the quality of the results.

The numerical discretization of differential operators was implemented up to second-order accuracy in space and time. Second-order accuracy in space arises by postulating a linear spatial variation of unknown quantities. We prevented spurious numerical oscillations intrinsic to second-order methods by limiting the face flux $F_f \simeq u_f \cdot s_f$ arising from the convective term in the momentum equation (2.2) with a van Leer total variation diminishing scheme (see Jasak, Weller & Gosman 1999). Besides, in the case of steady numerical simulations used in §§ A.2 and A.3 as basic flow, for which the temporal variation in (2.2) vanishes, the set of discretized equations (2.1)–(2.2) constitutes a saddle-point problem that was solved with SIMPLE with under-relaxation (see Patankar & Spalding 1972; Benzi, Golub & Liesen 2005). On the other hand, for unsteady numerical simulations, the second-order, two time-level Crank–Nicholson scheme is blended with an Euler scheme in order to solve the discretized momentum equation implicitly (separately and with nonlinear terms lagged). Since we are interested in temporal accuracy, i.e. small time steps, the pressure-implicit with splitting of operators (PISO) solver was adopted in this work (see Issa 1986; Ferziger & Perić 2002), and the lagged new time-level values were updated, solving all the equations once per time step. This leads to a Courant–Friedrichs–Lewy (CFL) stability condition and, therefore, the time step was calculated and adjusted during the numerical simulation. The Courant number at the nth-time step, denoted by t^n, is defined as $CFL = (|u_f^n \cdot s_f|)/(d_f \cdot s_f) \Delta t^n \leqslant 0.5$. As an example, considering the current mesh and setting a time step of $\Delta t = 10^{-2}$ for a Reynolds number of 415, we obtained a mean Courant number of approximately 0.1 and a maximum value of 0.5, although for Reynolds numbers greater than 500 we limited the maximum Courant

number to 0.2 in our simulations. Note that the time steps used are similar to those employed in related works, where they were varied from 2.5×10^{-3} for a Reynolds number of $Re = 1000$ (Tomboulides & Orszag 2000) to 5×10^{-2} for $Re = 300$ (Johnson & Patel 1999). In doing so, the pressure–velocity coupling is much stronger than the nonlinear coupling that arises from the nonlinear convection term. The latter result was corroborated by increasing the number of outer loops in the PISO solver from 1 to 3 at several Reynolds numbers, showing nearly identical results.

A.2. *Global stability analysis*

In addition to three-dimensional numerical simulations of the wake, we also carried out linear global and local stability analyses to describe the stability properties of the flow. The basic axisymmetric steady flow, used for both local and global stability analyses, was calculated using the finite-volume numerical code described in §§ 2.1 and A.1.

Starting with the incompressible unsteady equations (2.1) and (2.2), to perform the global stability analysis, the flow was decomposed into a basic steady-state field, and a perturbed field as

$$(\boldsymbol{u}, p) = (\boldsymbol{U} + \boldsymbol{u}', P + p'), \tag{A 1}$$

where $\boldsymbol{U} = [U(r, z)\, e_r, 0\, e_\theta, W(r, z)\, e_z]$ and $P(r, z)$ are the velocity and pressure fields of the basic axisymmetric-steady flow, and $\boldsymbol{u}' = (u', v', w')$ and p' represent the small amplitude, unsteady velocity and pressure perturbation fields, respectively.

After substituting (A 1) into the incompressible Navier–Stokes equations and withholding only the first-order terms, we obtain

$$\nabla \cdot \boldsymbol{u}' = 0, \tag{A 2}$$

$$\boldsymbol{U} \cdot \nabla \boldsymbol{u}' + \boldsymbol{u}' \cdot \nabla \boldsymbol{U} + \nabla p' - \frac{1}{Re} \nabla^2 \boldsymbol{u}' = -\frac{\partial \boldsymbol{u}'}{\partial t}. \tag{A 3}$$

Equations (A 2) and (A 3) can be formally expressed as

$$\mathscr{A} \boldsymbol{q} = \partial/\partial t \, \mathscr{B} \boldsymbol{q}, \tag{A 4}$$

where $\boldsymbol{q} = [\boldsymbol{u}', p']^{\mathrm{T}}$ represents the total disturbance field, with $\mathscr{A}$ and $\mathscr{B}$ being linear matrix operators. Assuming both time and azimuthal exponential dependences, solutions for $\boldsymbol{q}$ of the form

$$\boldsymbol{q} = [\hat{\boldsymbol{u}}(r, z), \hat{p}(r, z)]^{\mathrm{T}} e^{\sigma t + \mathrm{i} m \theta} = \hat{\boldsymbol{q}}(r, z)\, e^{\sigma t + \mathrm{i} m \theta} \tag{A 5}$$

can be sought, where the variables with a hat, $\hat{\boldsymbol{u}}$, $\hat{p}$ and $\hat{\boldsymbol{q}}$, represent the eigenfunctions, m is the azimuthal mode, and $\sigma = \sigma_r + \mathrm{i} \sigma_i$ with σ_r the growth rate of the global mode and σ_i its angular frequency. Substituting (A 5) into (A 4) with the boundary conditions:

$$0 < r < 0.5, \quad z = 0: \quad \hat{u} = \hat{v} = \hat{w} = 0, \tag{A 6}$$

$$r = 0.5, \quad -L/D + 1 \leqslant z \leqslant 0: \quad \hat{u} = \hat{v} = \hat{w} = 0, \tag{A 7}$$

$$0.5 < r \leqslant 10, \quad z = -L/D + 1: \quad \hat{u} = \hat{v} = \hat{w} = 0, \tag{A 8}$$

$$r = 10, \quad -L/D + 1 < z < 50: \quad \hat{u} = \hat{v} = \partial \hat{w}/\partial r = 0, \tag{A 9}$$

$$0 < r \leqslant 10, \quad z = 50: \quad \hat{p} = \boldsymbol{n} \cdot \nabla \hat{\boldsymbol{u}} = 0, \tag{A 10}$$

$$r = 0, \quad 0 \leqslant z \leqslant 50: \quad \begin{cases} |m| = 1, & \hat{u} \pm \mathrm{i}\hat{v} = 2\,\partial\hat{u}/\partial r \pm \mathrm{i}\,\partial\hat{v}/\partial r = \hat{w} = 0, \\ |m| = 0, & \hat{u} = \hat{v} = \partial\hat{w}/\partial r = 0, \\ |m| > 1, & \hat{u} = \hat{v} = \hat{w} = 0, \end{cases} \tag{A 11}$$
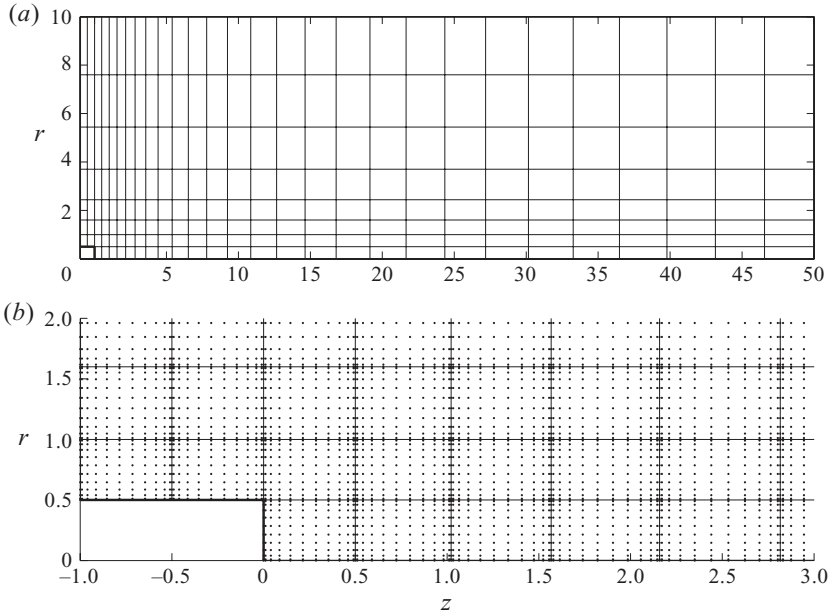
FIGURE 23. (*a*) Domain decomposition into 222 subdomains, where the thin solid lines correspond to the subdomain boundaries. (*b*) Grid detail close to the body for 12×12 nodes distributed according to the Gauss–Lobatto–Chebyshev points in each subdomain for a body of $L/D = 2$.

yields a generalized eigenvalue problem, which after discretizing can be written as

$$\mathscr{A}_m \hat{\boldsymbol{q}} = \sigma \mathscr{B}_m \hat{\boldsymbol{q}}, \qquad (A\,12)$$

where $\mathscr{A}_m$ and $\mathscr{B}_m$ are matrices of order $4n_g \times 4n_g$, n_g being the number of grid points. Note that $z = 0$ corresponds to the body base, and $z = -L/D + 1$ in (A 7)–(A 9) indicates the position upstream from the base where the nose of the body ends (see figure 23). As discretization technique we used the Chebyshev collocation–decomposition method that, basically, consists of dividing the computational domain into a block-structured grid with fictitious overlapping interfaces. More details about the numerical scheme can be found in Sanmiguel-Rojas *et al.* (2009), where it has recently been shown that a mesh of 222 subdomains (see figure 23) and 12×12 nodes distributed according to the Gauss–Lobatto–Chebyshev points in each subdomain, which represents a total number of spectral nodes of $n_g = 27\,259$, is enough to obtain a good convergence of the eigenvalues for a length of 50 behind the base of the body.

A.3. *Local linear stability analysis*

The local stability analysis of the wake presented in this section follows the same lines as that performed in Sevilla & Martínez-Bazán (2004). It is based on the assumption that the stability of the actual non-parallel basic flow is governed, at leading order, by the stability problem associated with the fictitious parallel flow obtained by extending the local basic-flow axial velocity profile to plus and minus streamwise infinity. However, in contrast with the inviscid analysis performed in Sevilla & Martínez-Bazán (2004), here viscous terms have been retained in the stability equations due to the smaller values of the Reynolds number analysed in this work. The local eigenvalue problem is obtained by linearizing the incompressible Navier–Stokes

equations around the basic parallel flow $W(r)\mathbf{e}_z$, and searching for modal solutions of the form $[\mathrm{i}\hat{u}(r), \hat{v}(r), \hat{w}(r), \hat{p}(r)]\exp[\sigma_l t + \mathrm{i}(kz + m\theta)]$ for the linearized velocity and pressure fields, where $k = k_r + \mathrm{i}k_i$ stands for the axial wavenumber, m denotes the azimuthal number and $\sigma_l = \sigma_{lr} + \mathrm{i}\sigma_{li}$ is the local angular frequency, respectively, and $(\hat{u}, \hat{v}, \hat{w}, \hat{p})$ are the radial eigenfunctions representing the complex amplitudes of the corresponding linearized fields. The linear system for the normal modes is

$$\frac{\mathrm{d}(r\hat{u})}{\mathrm{d}r} + m\hat{v} + kr\hat{w} = 0, \quad \text{(A 13)}$$

$$(\mathrm{i}\sigma_l - kW)\hat{u} + \frac{\mathrm{d}\hat{p}}{\mathrm{d}r} - \frac{\mathrm{i}}{Re}\left[\frac{\mathrm{d}^2\hat{u}}{\mathrm{d}r^2} + \frac{1}{r}\frac{\mathrm{d}\hat{u}}{\mathrm{d}r} - \left(k^2 + \frac{m^2+1}{r^2}\right)\hat{u} - \frac{2m}{r^2}\hat{v}\right] = 0, \quad \text{(A 14)}$$

$$(\mathrm{i}\sigma_l - kW)\hat{v} - \frac{m}{r}\hat{p} - \frac{\mathrm{i}}{Re}\left[\frac{\mathrm{d}^2\hat{v}}{\mathrm{d}r^2} + \frac{1}{r}\frac{\mathrm{d}\hat{v}}{\mathrm{d}r} - \left(k^2 + \frac{m^2+1}{r^2}\right)\hat{v} - \frac{2m}{r^2}\hat{u}\right] = 0, \quad \text{(A 15)}$$

$$(\mathrm{i}\sigma_l - kW)\hat{w} - \frac{\partial W}{\partial r}\hat{u} - k\hat{p} - \frac{\mathrm{i}}{Re}\left[\frac{\mathrm{d}^2\hat{w}}{\mathrm{d}r^2} + \frac{1}{r}\frac{\mathrm{d}\hat{w}}{\mathrm{d}r} - \left(k^2 + \frac{m^2}{r^2}\right)\hat{w}\right] = 0. \quad \text{(A 16)}$$

Equations (A 13)–(A 16) are supplemented with the boundary conditions

$$r \to \infty : \quad \hat{u} = \hat{v} = \hat{w} = \hat{p} = 0, \quad \text{(A 17)}$$

$$r = 0 : \quad \begin{cases} |m| = 0, & \hat{u} = \hat{v} = \partial\hat{w}/\partial r = 0, \\ |m| = 1, & \hat{u} \pm \hat{v} = 2\,\partial\hat{u}/\partial r \pm \partial\hat{v}/\partial r = \hat{w} = 0, \\ |m| > 1, & \hat{u} = \hat{v} = \hat{w} = 0. \end{cases} \quad \text{(A 18)}$$

A Chebyshev collocation technique was used to solve the eigenvalue problem (A 13)–(A 18), together with the coordinate transformation used by Lesshafft & Huerre (2007), $r = r_c(1 - \xi)/(1 - \xi^2 + 2r_c/r_{max})$, where r_c is a scale factor, which maps the canonical interval $\xi \in (-1, 1)$ onto the radial interval $r \in (0, r_{max})$. Thus, derivatives were computed in physical space by means of the chain rule $\mathrm{d}/\mathrm{d}r = \mathrm{d}\xi/\mathrm{d}r\,\mathrm{d}/\mathrm{d}\xi$, where $\mathrm{d}/\mathrm{d}\xi$ represents the standard Chebyshev differentiation matrix. Note that, although the far-field boundary conditions (A 17) were imposed at a finite value of the radial coordinate, r_{max}, it was carefully checked that r_{max} was large enough so that the resulting eigenvalues corresponded to their asymptotic limits as $r_{max} \to \infty$. Typically, we used $n_l = 200$ collocation points and a value of $r_{max} = 200$. In this work, as in Sevilla & Martínez-Bazán (2004), we were mainly interested in studying the convective or absolute character of the local instability as a function of the streamwise position z. To that end, we employed the iterative technique introduced by Monkewitz & Sohn (1988) for finding saddle points of the dispersion relation, i.e. eigenvalues $(\sigma_l^{(0)}, k^{(0)})$ satisfying (A 13)–(A 18) together with the zero group velocity condition $\mathrm{d}\sigma_l/\mathrm{d}k = 0$. Although the details are in Monkewitz & Sohn (1988), we point out here that the iterative procedure reconstructs the local form of the dispersion relation around a saddle point, $k^\pm - k^{(0)} = \pm a(\sigma_l - \sigma_l^{(0)})^{1/2} + b(\sigma_l - \sigma_l^{(0)})$, through the computation of the four complex constants $(k^{(0)}, \sigma_l^{(0)}, a, b)$. In this equation, the plus and minus signs correspond to the pair of spatial branches which interact at the saddle point $(\sigma_l^{(0)}, k^{(0)})$. The four equations needed to determine the constants are obtained by computing $k^\pm$ for two different values of σ_l close to the branch point $\sigma_l^{(0)}$. Thus, at each iteration level, the spatial eigenvalue problem $k = k(\sigma_l)$ is solved four times. This was accomplished here thanks to the use of the companion matrix method, which allowed us to find k by means of the $7n_l \times 7n_l$ matrix eigenvalue problem $\mathscr{A}_l\boldsymbol{q}_l = k\,\mathscr{B}_l\,\boldsymbol{q}_l$, where the vector $\boldsymbol{q}_l = (\hat{u}, \hat{v}, \hat{w}, \hat{p}, k\hat{u}, k\hat{v}, k\hat{w})^{\mathrm{T}}$, and the matrices $\mathscr{A}_l$ and $\mathscr{B}_l$ were obtained through the
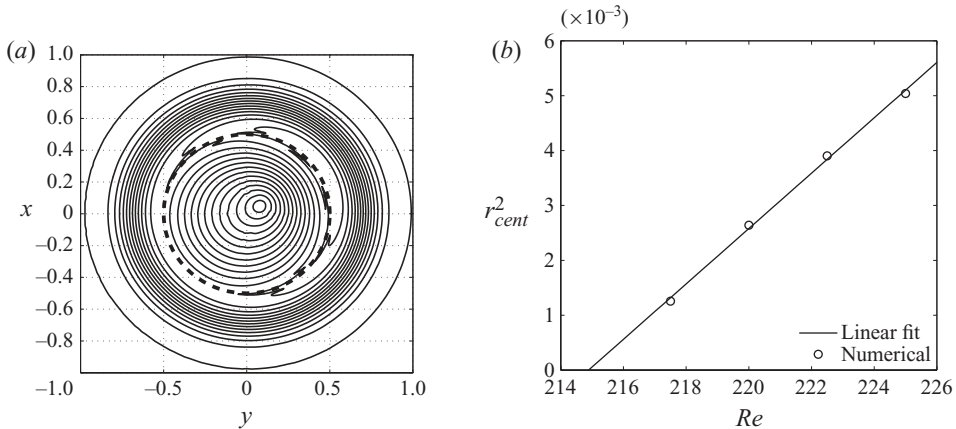
FIGURE 24. (*a*) Isolines of the vorticity magnitude at $z = 2$ for a body of $L/D = 1$ at $Re = 220$ showing the centroid eccentricity, and (*b*) squared centroid eccentricity versus the Reynolds number at $z = 2$ (circles), together with a linear fit (solid line), illustrating the method used to determine Re_{cs}^{3d}. The dashed line in (*a*) represents the body base.

spectral collocation method described above. The local instability at a given station z is convective if the *absolute growth rate*, given by the real part of $\sigma_l^{(0)}$, is negative, $\sigma_{lr}^{(0)} < 0$, while it is absolute if $\sigma_{lr}^{(0)} > 0$, and the flow is expected to be globally stable if it is convectively unstable everywhere, $\sigma_{lr}^{(0)}(z) < 0 \ \forall z$.

Appendix B. Methods used to determine Re_{cs}^{3d}, Re_{co}^{3d} and C_{b1}^*

This appendix provides additional information about the different methods used to determine the critical Reynolds numbers for the steady and the oscillatory bifurcations from the direct numerical simulations, denoted Re_{cs}^{3d} and Re_{co}^{3d} respectively.

In order to calculate the critical Reynolds number corresponding to the first steady bifurcation from the direct numerical simulations, Re_{cs}^{3d}, we followed Mullin *et al.* (2009) and made use of the linear dependence of the squared eccentricity of the vorticity contours, denoted by r_{cent}^2, on $Re - Re_{cs}^{3d}$. Thus, we plotted the evolution of r_{cent}^2 with the Reynolds number obtained at a fixed position to determine Re_{cs}^{3d} by linear regression. An example of the procedure is shown in figure 24, where figure 24(*a*) clearly shows that the vorticity magnitude exhibits an eccentricity for a flow with $Re = 220$ past a body with length-to-diameter ratio $L/D = 1$ in this particular case. Furthermore, figure 24(*b*) confirms that the squared eccentricity varies linearly with $Re - Re_{cs}^{3d}$ and provides a critical value of $Re_{cs}^{3d} \simeq 215$. Similarly, for a body of the length-to-diameter ratio $L/D = 2$, we obtained $Re_{cs}^{3d} \simeq 319$.

To determine the critical value Re_{co}^{3d} for the onset of vortex shedding from the numerical simulations reported in §2.1, we used two different techniques. As stated in the previous section, at $Re = 415$ we observed the periodic shedding of vortices for a body with length-to-diameter ratio $L/D = 2$. Thus, we used this perturbed flow as initial condition for a numerical simulation with a Reynolds number decreased down to $Re = 410$, which is stable because the streamwise perturbation velocity is attenuated until it ultimately vanishes (see figure 25a). Finally, the ensuing decay rate is determined by fitting the disturbance amplitude to an exponential function of time (see figure 25b), which provides a decay rate of -0.004835. Similarly, we ran a new
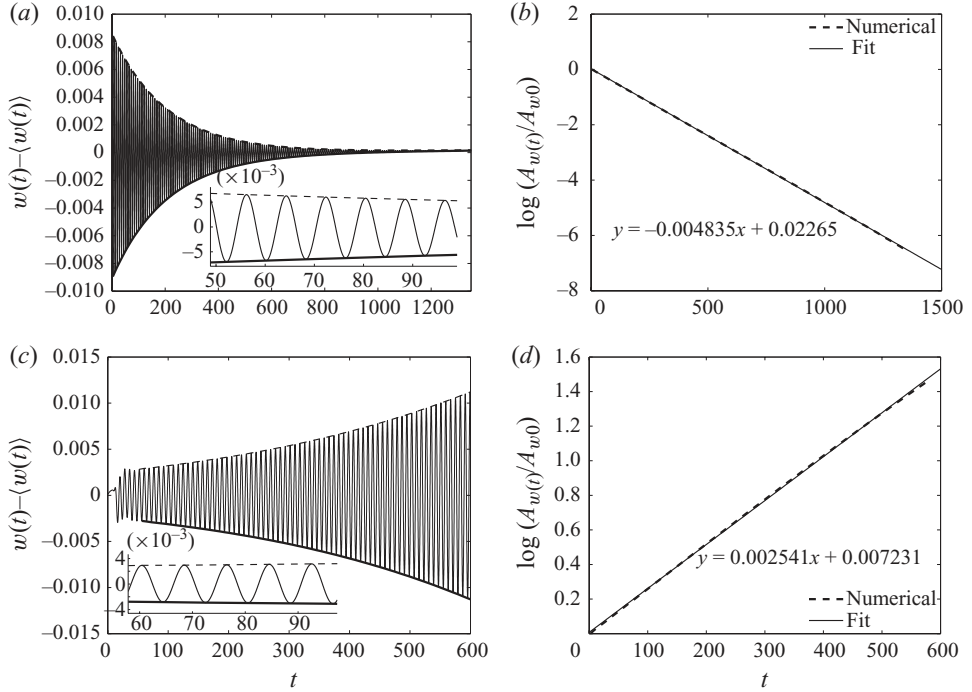
FIGURE 25. Determination of the growth/decay rate (close to criticality) from the direct numerical simulation of the temporal evolution of small disturbances in the streamwise velocity for a body of $L/D = 2$. Plots (a) and (c) show the transient behaviour of the streamwise velocity fluctuations, $w(t) - \langle w(t) \rangle$, at $z = 7$ at Reynolds numbers $Re = 410$ and $Re = 414$, respectively, and (b) and (d) display the corresponding exponential fit of the disturbance amplitude as a function of time t.

simulation at $Re = 414$ using the solution for $Re = 410$ at $t = 1300$ as initial condition, which still contains an infinitesimal disturbance, and observed the growth of the oscillatory mode, as shown in figure 25(c). In this case, the ensuing amplification factor is 0.002541 (see figure 25d). Subsequently, we determined that the instability threshold was $Re_{co}^{3d} = 412.62$ by linear interpolation of the amplification factors (Ghidersa & Dušek 2000) given at $Re = 410$ and 414. Following the same procedure, we obtained $Re_{co}^{3d} = 254.37$ for a body of the length-to-diameter ratio $L/D = 1$, which is slightly lower than the critical value corresponding to the sphere ($Re_{co}^{exp} \approx 270$ given by Goldburg & Florsheim 1966) and greater than the values obtained for other blunt-based bodies of revolution like a hemisphere ($Re_{co}^{3d} \approx 210$–220 given by Kim & Choi 2003) and cones where Re_{co}^{exp} varies from 155 to 170, depending on the cone angle (Goldburg & Florsheim 1966; Yaginuma & Itō 2008). Note that the relative difference between the critical values of the Reynolds number associated with the steady state, Re_{cs}^{3d}, and reflectional symmetry-preserving, Re_{co}^{3d}, modes, $\Delta^{3d} = (R_{co}^{3d} - Re_{cs}^{3d})/Re_{cs}^{3d}$, does not decrease substantially for the shortest body, since the physical values of Δ^{3d} vary from 0.29 for $L/D = 2$ to 0.18 for $L/D = 1$.

With the aim of determining the uncertainty associated with the different methods used to calculate the value of Re_{co}^{3d} in the numerical simulations and in the experiments, we have also followed the Stuart–Landau procedure in the case of a body with length-to-diameter ratio of $L/D = 2$. Figure 13(b) readily shows that the squared amplitude of the tangential velocity decreases linearly as the Reynolds number decreases, providing
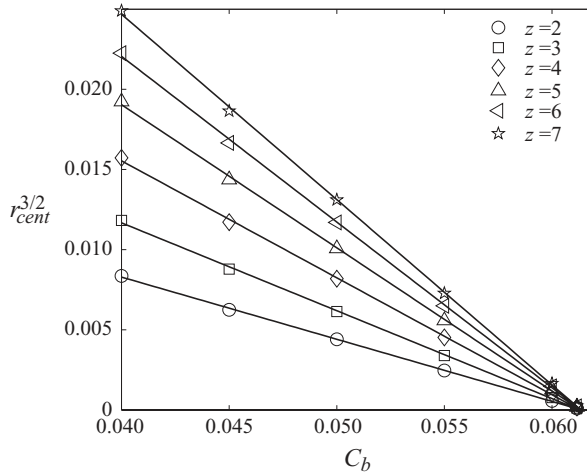
FIGURE 26. Determination of the critical base bleed coefficient C_{b1}^* by interpolation of the centroid eccentricity r_{cent} as a function of C_b for $Re = 450$ and a body of $L/D = 2$ at different downstream positions.

a critical Reynolds number of $Re_{co}^{3d} \simeq 413.17$, which is nearly identical to the value of $Re_{co}^{3d} = 412.62$ given by the procedure described above. Thus, we adopted $Re_{co}^{3d} \simeq 413$ as the critical value.

Finally, to obtain the critical value of the base bleed coefficient C_{b1}^*, which re-stabilizes the steady bifurcation, we followed an approach similar to that employed to determine Re_{cs}^{3d}. In this case, we took advantage of the fact that the centroid eccentricity r_{cent} depends linearly on $(C_{b1}^* - C_b)^{2/3}$, as depicted in figure 26, where $r_{cent}^{3/2}$ is plotted as a function of C_b for several values of the downstream position z in the particular case of $L/D = 2$ and $Re = 450$. In this case, a linear fit provides the value $C_{b1}^* = 0.0613$. The application of a similar procedure to other values of Re provided the values of C_{b1}^*, as shown by circles in figure 19.

REFERENCES

ACHENBACH, E. 1974 Vortex shedding from spheres. *J. Fluid Mech.* **62** (2), 209–221.

ARKAS, D. R. & REDEKOPP, L. G. 2004 Aspects of wake vortex control through base blowing/suction. *Phys. Fluids* **16**, 452–456.

AUGUSTE, F., FABRE, D. & MAGNAUDET, J. 2010 Bifurcations in the wake of a thick circular disk. *Theor. Comput. Fluid Dyn.* **24**, 305–313.

BAGHERI, S., SCHLATTER, P., SCHMID, P. J. & HENNINGSON, D. 2009 Global stability of a jet in cross-flow. *J. Fluid Mech.* **624**, 33–44.

BEARMAN, P. W. 1967 The effect of base bleed on the flow behind a two-dimensional model with a blunt trailing edge. *Aeronaut. Q.* **18**, 207–224.

BENZI, M., GOLUB, G. H. & LIESEN, J. 2005 Numerical solution of saddle point problems. *Acta Numerica* **14**, 1–137.

BERGER, E., SCHOLZ, D. & SCHUMM, M. 1990 Coherent vortex structures in the wake of a sphere and a circular disk at rest and under forced vibrations. *J. Fluid Struct.* **4**, 231–257.

BOUCHET, G., MEBAREK, M. & DUŠEK, J. 2006 Hydrodynamic forces acting on a rigid fixed sphere in early transition regimes. *Eur. J. Mech.* B/*Fluids* **25**, 321–336.

BRÜCKNER, C. 2001 Spatio-temporal reconstruction of vortex dynamics in axisymmetric wakes. *J. Fluids Struct.* **15**, 543–554.

CHOI, H., JEON, W.-P. & KIM, J. 2008 Control of flow over a bluff body. *Annu. Rev. Fluid Mech.* **40**, 113–139.

FABRE, D., AUGUSTE, F. & MAGNAUDET, J. 2008 Bifurcations and symmetry breaking in the wake of axisymmetric bodies. *Phys. Fluids* **20**, 051702.

FERZIGER, J. H. & PERIĆ, M. 2002 *Computational Methods for Fluid Dynamics*. Springer.

FUCHS, H. V., MERCKER, E. & MICHEL, U. 1979 Large-scale coherent structures in the wake of axisymmetric bodies. *J. Fluid Mech.* **93** (1), 185–207.

GHIDERSA, B. & DUŠEK, J. 2000 Breaking of axisymmetry and onset of unsteadiness in the wake of a sphere. *J. Fluid Mech.* **423**, 33–69.

GOLDBURG, A. & FLORSHEIM, B. H. 1966 Transition and Strouhal number for the incompressible wake of various bodies. *Phys. Fluids* **9** (1), 45–50.

GOLUBITSKY, M., STEWART, I. & SCHAEFFER, D. G. 1988 *Singularities and Groups in Bifurcation Theory*. Springer.

HAMMOND, D. A. & REDEKOPP, L. G. 1997 Global dynamics of symmetric and asymmetric wakes. *J. Fluid Mech.* **331**, 231–260.

HANNEMANN, K. & OERTEL, H. JR 1989 Numerical simulation of the absolutely and convectively unstable wake. *J. Fluid Mech.* **199**, 55–88.

ISSA, R. I. 1986 Solution of the implicitly discretised fluid flow equations by operator-splitting. *J. Comput. Phys.* **62**, 40–65.

JASAK, H. 1996 Error analysis and estimation in the finite volume method with applications to fluid flows. PhD thesis, Imperial College, University of London.

JASAK, H., WELLER, H. G. & GOSMAN, A. D. 1999 High resolution NVD differencing scheme for arbitrarily unstructured meshes. *Intl J. Numer. Meth. Fluids* **31**, 431–449.

JOHNSON, T. A. & PATEL, V. C. 1999 Flow past a sphere up to a Reynolds number of 300. *J. Fluid Mech.* **378**, 19–70.

KIM, D. & CHOI, H. 2003 Laminar flow past a hemisphere. *Phys. Fluids* **15** (8), 2457–2460.

KIM, H. J. & DURBIN, P. A. 1988 Observations of the frequencies in a sphere wake and of drag increase by acoustic excitation. *Phys. Fluids* **31** (11), 3260–3265.

KUZNETSOV, Y. A. 1995 *Elements of Applied Bifurcation Theory*. Springer.

LESSHAFFT, L. & HUERRE, P. 2007 Linear impulse response in hot round jets. *Phys. Fluids* **19**, 024102.

LEVI, E. 1980 Three-dimensional wakes: origin and evolution. *J. Engng Mech.* **106**, 659–676.

MAGNAUDET, J. & MOUGIN, G. 2007 Wake instability of a fixed spheroidal bubble. *J. Fluid Mech.* **572**, 311–337.

MARGAVEY, R. & BISHOP, R. L. 1961 Transition ranges for three-dimensional wakes. *Can. J. Phys.* **39**, 1418–1422.

MELIGA, P., CHOMAZ, J.-M. & SIPP, D. 2009 Global mode interaction and pattern selection in the wake of a disk: a weakly nonlinear expansion. *J. Fluid Mech.* **633**, 159–189.

MELIGA, P., SIPP, D. & CHOMAZ, J.-M. 2010a Effect of compressibility on the global stability of axisymmetric wake flows. *J. Fluid Mech.* **660**, 499–526.

MELIGA, P., SIPP, D. & CHOMAZ, J.-M. 2010b Open-loop control of compressible afterbody flows using adjoint methods. *Phys. Fluids* **22**, 054109.

MONKEWITZ, P. A. 1988 A note on vortex shedding from axisymmetric bluff bodies. *J. Fluid Mech.* **192**, 561–575.

MONKEWITZ, P. A. & SOHN, K. D. 1988 Absolute instability in hot jets. *AIAA J.* **28**, 911–916.

MULLIN, T., SEDDON, J. R. T., MANTLE, M. D. & SEDERMAN, A. J. 2009 Bifurcation phenomena in the flow through a sudden expansion in a circular pipe. *Phys. Fluids* **21**, 014110.

NATARAJAN, R. & ACRIVOS, A. 1993 The instability of the steady flow past spheres and disks. *J. Fluid Mech.* **254**, 323–344.

OERTEL, H. JR 1990 Wakes behind blunt bodies. *Annu. Rev. Fluid Mech.* **22**, 539–564.

ORMIÉRES, D. & PROVANSAL, M. 1999 Transition to turbulence in the wake of a sphere. *Phys. Rev. Lett.* **83** (1), 80–83.

PATANKAR, S. V. & SPALDING, D. B. 1972 A calculation procedure for heat, mass and momentum transfer in three-dimensional parabolic flows. *Intl J. Heat Mass Transfer* **15** (10), 1787–1806.

PIER, B. 2008 Local and global instabilities in the wake of a sphere. *J. Fluid Mech.* **603**, 39–61.

PIER, B., HUERRE, P., CHOMAZ, J.-M. & COUAIRON, A. 1998 Steep nonlinear global modes in spatially developing media. *Phys. Fluids* **10** (10), 2433–2435.

PRASAD, A. & WILLIAMSON, C. 1997 The instability of the shear layer separating from a bluff body. *J. Fluid Mech.* **333**, 375–402.

RHIE, C. M. & CHOW, W. L. 1983 Numerical study of the turbulent flow past an airfoil with trailing edge separation. *AIAA J.* **21** (11), 1525–1532.

SAKAMOTO, H. & HANIU, H. 1990 A study of vortex shedding from spheres in a uniform flow. *J. Fluid Struct.* **112**, 386–392.

SANMIGUEL-ROJAS, E., SEVILLA, A., MARTÍNEZ-BAZÁN, C. & CHOMAZ, J.-M. 2009 Global mode analysis of axisymmetric bluff-body wakes: stabilization by base bleed. *Phys. Fluids* **21**, 114102.

SCHMID, P. J. 2010 Dynamic mode decomposition of numerical and experimental data. *J. Fluid Mech.* **656**, 5–28.

SCHOUVEILER, L. & PROVANSAL, M. 2002 Self-sustained oscillations in the wake of a sphere. *Phys. Fluids* **14** (11), 3846–3854.

SCHUMM, M., BERGER, E. & MONKEWITZ, P. A. 1994 Self-excited oscillations in the wake of two-dimensional bluff bodies and their control. *J. Fluid Mech.* **271**, 17–53.

SCHWARZ, V. & BESTEK, H. 1994 Numerical simulation of nonlinear waves in the wake of an axisymmetric bluff body. In *25th AIAA Fluid Dynamics Conference*. *AIAA Paper* 94-2285.

SEVILLA, A. & MARTÍNEZ-BAZÁN, C. 2004 Vortex shedding in high Reynolds number axisymmetric bluff-body wakes: Local linear instability and global bleed control. *Phys. Fluids* **16**, 3460–3469.

SEVILLA, A. & MARTÍNEZ-BAZÁN, C. 2006 A note on the stabilization of bluff-body wakes by low density base bleed. *Phys. Fluids* **18**, 098102.

SHENOY, A. R. & KLEINSTREUER, C. 2008 Flow over a thin circular disk at low to moderate Reynolds numbers. *J. Fluid Mech.* **605**, 253–262.

STEWART, B. E., THOMPSON, M. C., LEWEKE, T. & HOURIGAN, K. 2010 Numerical and experimental studies of the rolling sphere wake. *J. Fluid Mech.* **643**, 137–162.

TANEDA, S. 1956 Experimental investigation of the wake behind a sphere at low Reynolds numbers. *J. Phys. Soc. Japan* **11**, 1104–1108.

TANEDA, S. 1978 Visual observations of the flow past a sphere at Reynolds numbers between 10^4 and 10^6. *J. Fluid Mech.* **85** (1), 187–192.

THOMPSON, M. C., LEWEKE, T. & PROVANSAL, M. 2001 Kinematics and dynamics of sphere wake transition. *J. Fluids Struct.* **15**, 575–585.

TOMBOULIDES, A. G. & ORSZAG, S. A. 2000 Numerical investigation of transitional and weak turbulent flow past a sphere. *J. Fluid Mech.* **416**, 45–73.

WILLIAMSON, C. H. K. 1996 Vortex dynamics in the cylinder wake. *Annu. Rev. Fluid Mech.* **28**, 477–539.

WOOD, C. J. 1964 The effect of base bleed on a periodic wake. *J. R. Aeronaut. Soc.* **68**, 477–482.

WOOD, C. J. 1967 Visualization of an incompressible wake with base bleed. *J. Fluid Mech.* **29**, 259–272.

YAGINUMA, T. & ITŌ, H. 2008 Drag and wakes of freely falling 60° cones at intermediate Reynolds numbers. *Phys. Fluids* **20** (11), 117102.